THE UNIVERSITY *of* EDINBURGH

Edinburgh Research Explorer

Characteristics of the impact pressure of debris flows

OPEN ACCESS

Characteristics of the impact pressure of debris flows

Hongchao Zheng[1], Zhenming Shi[1], Tjalling de Haas[2], Danyi Shen[1*], Kevin J Hanley[3], Bo Li[1]

[1]Department of Geotechnical Engineering, College of Civil Engineering, Tongji University, China

[2] Department of Physical Geography, Utrecht University, The Netherlands

[3]School of Engineering, Institute for Infrastructure and Environment, The University of Edinburgh, United Kingdom

*corresponding author: Danyi Shen, E–mail: 1107sdy@tongji.edu.cn

Abstract

Debris flows are common geological hazards in mountainous regions worldwide. Predicting the impact pressure of debris flows is of major importance for hazard mitigation. Here, we experimentally investigate the impact characteristics of debris flows by varying the concentrations of debris grains and slurry. The measured impact pressure signal is decomposed into a stationary mean pressure and a fluctuating pressure through empirical mode decomposition. The stationary mean pressure of low frequency is caused by the thrusting of bulk flow while the fluctuating pressure of high frequency is induced by the collision of coarse debris grains, revealed by comparing the features of impact pressure spectra of pure slurries and debris flows. The peak stationary mean pressure and the peak fluctuating pressure first increase and then decrease with the slurry density. The basal frictional resistance is reduced by the nonequilibrium pore-fluid pressure for debris flows with low-density slurry, which can increase the flow velocity and impact pressures. In contrast, the viscous flow of high-density slurry tends to reduce the flow velocity. The peak stationary mean pressures are well predicted by the Bernoulli equation and are related to the hydrostatic pressure and Froude number of the incident flow. The peak fluctuating pressures depend on the kinetic energy and degree of segregation of coarse grains. The maximum degree of segregation occurs at an intermediate value of slurry density due to the transition of flow regime and fluid drag stresses. Our results facilitate predicting the impact pressures of debris flows based on their physical properties.

Plain Language Summary

Debris flows are mixtures of muddy water, sand, gravels, and boulders which move down steep mountain creeks in an uncontrolled way. They are a major threat to human life, properties, and infrastructure in mountainous regions. Debris flows commonly consist of a flow nose made of coarse-grained particles and a flow body comprising finer-grained and more liquefied debris. It is very important to predict their impact pressures which are significantly influenced by their flow behavior. In this study, the measured impact pressures of experimental debris flows were decomposed into several components through a signal processing method. The low-frequency components of the signal originated from the bulk flow and the high-frequency components were caused by the coarse debris grains. This decomposition inspired us to predict separately the pressures induced by bulk flow and coarse debris grains to obtain the peak impact pressure of a debris flow.

Key Points:

(1) Stationary mean pressure and fluctuating pressure are obtained from the measured impact pressure signals

(2) Peak stationary mean pressures are predicted well with a jet model based on the Bernoulli equation

(3) The transition in the dependence of grain segregation on viscosity coincides with the transition of the flow rheology

1. Introduction

Debris flows are gravity-driven mass movements in mountainous regions [*Iverson,* 1997; *Pudasaini,* 2012]. Peak flow velocities of debris flows can surpass 10 m/s, and volumes can reach ~10^9 m^3 [e.g., *Iverson,* 2011]. Debris flows can cover floodplains, block rivers and deteriorate the regional ecological environment [*Takahashi,* 2007; *Zheng et al.,* 2018, 2021a]. They further pose a major threat to human life, properties, and infrastructure [*de Haas et al.,* 2015; *Kaitna et al.,* 2016; *Zheng et al.,* 2021b].

A fundamental problem in disaster prevention engineering is to determine the impact pressure exerted on structures by a debris flow [*Sovilla et al.,* 2008]. This task is difficult because the impact pressure of a debris flow depends on both solid and fluid stresses that influence their motion and govern their rheological properties [*de Haas et al.,* 2015, 2021]. Debris flows typically have a wide grain-size distribution including sediment particles ranging in size from clay to boulders [*Iverson,* 1997; *de Haas et al.,* 2021]. The heterogeneous grain distribution of a debris flow in the longitudinal direction can also affect their impact pressures [*McCoy et al.,* 2010].

Particle size segregation is a common feature of debris flows: coarse particles tend to migrate towards the front of the flow and fines towards the rear [*Kaitna et al.,* 2016; *Zheng et al.,* 2021c]. Flow behavior is altered in time and space, often causing a flow snout with high frictional resistance, flow fingering and levee formation [*Vallance and Savage,* 2000; *Gray and Kokelaar,* 2010; *Johnson et al.,* 2012; *de Haas et al.,* 2015; *Pudasaini and Fischer,* 2020]. The impact pressure of a debris flow can

be amplified as a result of a large concentration of coarse grains at the flow front [*Watanabe and Ikeya,* 1981; *Hungr et al.,* 1984; *Hu et al.,* 2011]. However, the relation between grain segregation and the impact pressure is still unclear.

Current debris-flow impact models can be classified into hydraulic and solid-collision models [*Hubl et al.,* 2009]. This twofold classification indicates the complexity of debris-flow processes, where the impact can either be caused by fluid-phase flow thrusting or a point-wise loading and the collision of coarse grains [*Scheidl et al.,* 2013]. The hydraulic models are further classified into hydrostatic and hydrodynamic models. In general, the hydrostatic model is expressed as:

$$p_{\text{peak}} = k\rho_b gh \tag{1}$$

Here, p_{peak} is the peak debris-flow impact pressure with the parameter k as an empirical factor; ρ_b and h are the density and depth of a debris flow. The hydrodynamic model based on the impulse–momentum theorem is expressed as

$$p_{\text{peak}} = \lambda\rho_b v^2 \tag{2}$$

with the impact coefficient λ and the flow velocity v. For the former, the peak impact pressure measured from hillslope debris flows is typically 2–50 times the equivalent static flow pressures [*Bugnion et al.,* 2012]. For the latter, the back-calculated λ for the hydrodynamic models ranges from 0.4 to 17.0 [*Scheidl et al.,* 2013]. These fitted parameters with a wide range bring great uncertainty to designs in disaster prevention engineering.

Debris flows generally contain 40% to 70% sediment particles by volume [*Pierson,* 2005; *de Haas et al.,* 2015]. The volume concentration of debris flows may

significantly affect the impact pressure based on the hydraulic and solid-collision models. The hydrostatic pressures exhibit a linear relationship with the volume concentration of debris flows. Meanwhile, the interstitial slurry of a debris flow can be highly viscous because of the suspension of clay and silt particles in the interstitial water [e.g., *Coussot,* 1988]. Viscous slurry may facilitate nonequilibrium pore-fluid pressures in the flow, thereby enhancing flow velocity and impact pressures by decreasing the inter-granular friction [*Hsu et al.,* 2014; *Iverson,* 2003] and dampening grain collisions [*Vallance and Savage,* 2000; *Kaitna et al.,* 2016]. Further research is therefore needed to investigate the independent effects of volume concentration of debris grains and ambient slurry on the debris-flow dynamics and impact pressures.

The measured impact pressure signals of debris flows are characterized by a stationary mean value superimposed by fluctuations [*Sovilla et al.,* 2008; *Hubl et al.,* 2009; *Hu et al.,* 2011; *Bugnion et al.,* 2012; *Scheidl et al.,* 2013; *Cui et al.,* 2015]. The local fluctuations can result from environmental noise, resonance frequency of measuring apparatus, point-wise loading or hard impact of coarse grains, etc. [*Bugnion et al.,* 2012; *Scheidl et al.,* 2013]. Filtering or moving average methods are usually adopted to eliminate the fluctuations of impact pressure, considering that the durations of oscillation are very short [*Bugnion et al.,* 2012; *Scheidl et al.,* 2013]. The peak impact pressures of debris flows are thus underestimated as a result of such filtering procedures. Instead, a comprehensive decomposition of fluctuation signals based on their specific sources can efficiently improve the prediction of actual impact pressures.

To fill the knowledge gaps regarding impact pressure characterization, we conduct impact experiments of debris flows with varying concentrations of debris grains and slurry. One goal of this study is to be able to predict impact pressures from fundamental flow properties. The measured impact pressure signal from each test is decomposed into a stationary mean pressure and local fluctuations from different sources through empirical mode decomposition (EMD) [*Huang et al.,* 1998]. Subsequently, we establish a jet model [*Song et al.,* 2021] to predict the stationary mean pressure. The degree of segregation of coarse grains is assessed by the impulse–momentum theorem [*Bugnion et al.,* 2012]. Finally, we discuss the fluctuating pressure, impact coefficient of debris flow and segregation of coarse grains associated with the transition of flow regime.

2. Methods

2.1 Debris-flow Materials

We conducted 15 impact tests of debris flows with varying debris-grain concentration C_d ranging from 0.40–0.48 and the slurry density ρ_s ranging from 1000–1350 kg/m^3 (Table 1). The debris grain composition (0.125–8 mm) of the experimental flows is similar to the composition of the "Inferno" type debris flows in the western Italian Alps, as shown in Figure 1 [*Tiranti et al.,* 2008]. The slurry in these flows was a mixture of water and hydrous kaolin (0.001–0.01 mm). Five additional tests (tests 1–5) were conducted with pure slurries, i.e., without debris grains, to compare the impact pressures with those of flows with the same slurry

density.

Table 1 Parameters for the different tests

Test	ρ_b (kg/m^3)	ρ_s (kg/m^3)	ρ_d (kg/m^3)	ρ_c (kg/m^3)	C_v	C_d
1	1000	1000	0	0	0.00	0
2	1100	1100	0	0	0.06	0
3	1200	1200	0	0	0.12	0
4	1300	1300	0	0	0.18	0
5	1350	1350	0	0	0.21	0
6	1680	1000	1080	227	0.40	0.40
7	1740	1100	1080	227	0.44	0.40
8	1800	1200	1080	227	0.47	0.40
9	1860	1300	1080	227	0.51	0.40
10	1890	1350	1080	227	0.52	0.40
11	1748	1000	1188	250	0.44	0.44
12	1804	1100	1188	250	0.47	0.44
13	1860	1200	1188	250	0.51	0.44
14	1916	1300	1188	250	0.54	0.44
15	1944	1350	1188	250	0.56	0.44
16	1816	1000	1296	272	0.48	0.48
17	1868	1100	1296	272	0.51	0.48
18	1920	1200	1296	272	0.54	0.48
19	1972	1300	1296	272	0.57	0.48
20	1998	1350	1296	272	0.59	0.48

Note: ρ_s and ρ_b are the densities of slurry and bulk flow, respectively. ρ_d and ρ_c are the dry densities of debris grains and coarse grains (5–8 mm), respectively. $\rho_d = \rho_g C_d$ where ρ_g is the solid particle density (2700 kg/m³) and C_d is the volume concentration of debris grains. C_v is the volume concentration of debris flow. $\rho_b = \rho_g C_v + \rho_w (1 - C_v)$, where ρ_w is the water density (1000 kg/m³).
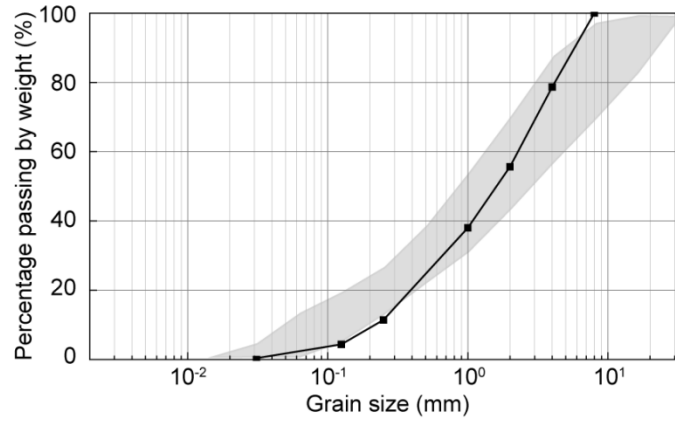

Figure 1. Compositions of debris grains (black line) in our tests and debris flows of the "Inferno" type in the Susa Valley of the Italian Alps (grey zone) [*Tiranti et al.,* 2008].

Slurry rheology was measured by a concentric cylinder viscometer (Anton Paar, MCR 301). The shear rate was 0.1–100 s⁻¹ at a temperature of 20 °C. The dynamic viscosity η of slurry increased significantly when the slurry density exceeded 1200 kg/m³ (Figure 2). We conducted direct shear tests (Humboldt, D-5780) to obtain the internal friction angle φ under a drainage condition, where the normal stresses were 50 kPa, 100 kPa, 150 kPa and 200 kPa, the shear rate was 1 mm/min, and the shear displacement was 60 mm.
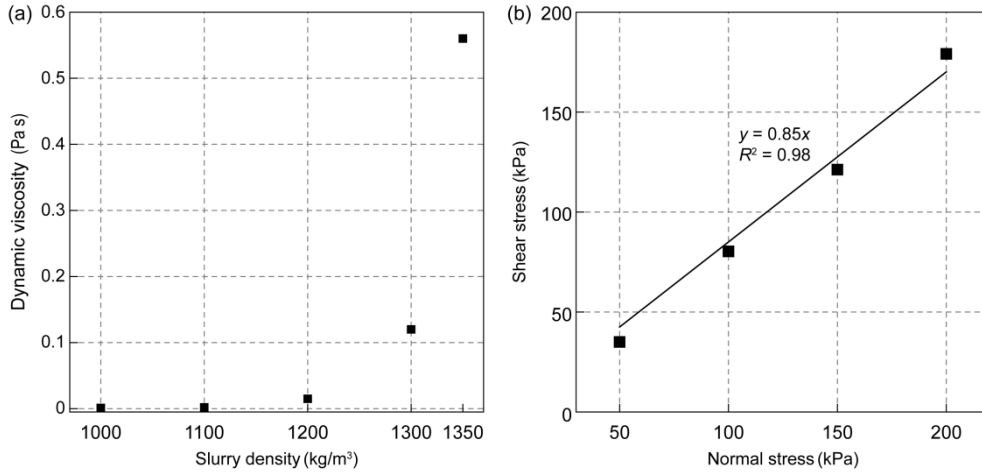
Figure 2. (a) Dynamic viscosity of slurry and (b) internal friction angle of debris. R^2 is the coefficient of determination for the linear regression in panel b.

2.2 Flume Setup

The experimental apparatus consisted of a mixing tank, a lever system and a straight-slope flume (Figures 3 and S1). The mixing tank with a volume of 0.07 m³ was used to store and mix the flow. A 0.5-m high vertical headgate was equipped to retain debris flow prior to its release. The headgate was constrained by a steel rod with a length of ~2.0 m, which was a part of the lever system. A rubber seal inside the headgate ensured that slurry in the mixing tank would not leak out.

The experimental flume had a height of 0.4 m, a width of 0.25 m, a length of 4.0 m and an angle θ of 27° to the horizontal plane. The flume sidewalls were made of transparent tempered glass, allowing the impact process of released flow to be observed. The bottom of the flume was pattern steel roughened by small bulges with a roughness height of 1.6 mm, matching the median diameter d_s of the debris flows to simulate natural channel roughness.
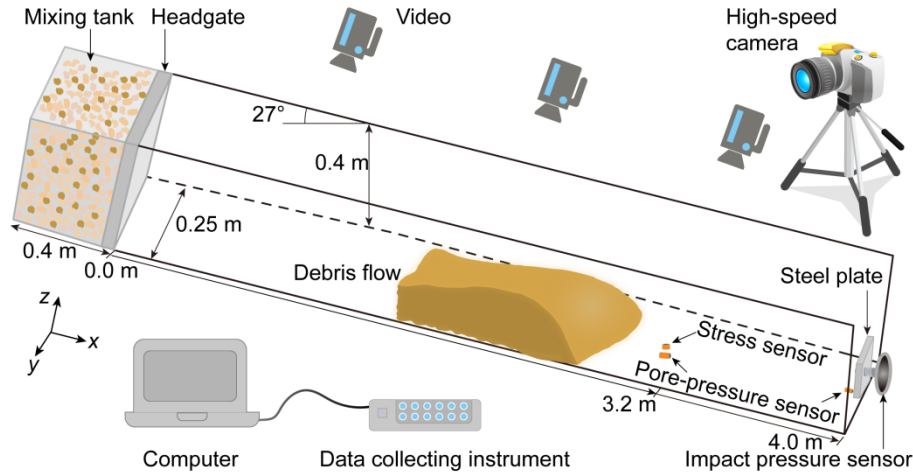
Figure 3. Schematic diagram of experimental apparatus.

The instruments used for investigating the impact process of debris flows are shown in Figure 3. A high-speed camera (i-SPEED7, iX Cameras) with a sample frequency of 200 Hz captured the flow characteristics in the cross-stream direction. The flow-front height h normal to the flume bottom and velocity v were obtained from the snapshots and scale plate. Three video cameras (GZ-R10BAC, JVC, 1920 x 1080 pixel) recorded the movement process of debris flows from the top of the flume. At x = 3.2 m we deployed pore pressure and stress sensors to measure the basal pore pressure and basal normal stress during debris flow propagation. At x = 4.0 m we deployed a pore-pressure sensor to measure the local dynamic fluid pressure during the impact process. The pore-pressure sensors were saturated and accommodated in a cavity on the flume bottom. Calibrations of pore pressure and stress sensors using static water pressures yielded regression line slopes that were both linear (determination coefficient R^2 > 0.99) and reproducible. A square steel panel (80 mm × 80 mm) was mounted to the strain-gauge sensor (Baumer, DLRP, range ±200 N) to bear the impact pressure of debris flows at the flume exit (Figure S2). A rigid block

was welded to the bottom of the flume to retain the strain-gauge sensor. The sample frequency of all electronic sensors was 2000 Hz.

2.3 Experimental Procedure

The volume of released flow V_0 for each test was 0.055 m^3. The debris was prepared as follows. First, the masses of debris grains and slurry in each flow were calculated according to the required concentration. Then, the debris material was poured into the mixing tank along with water injection. Finally, the debris was stirred by two blenders prior to and during release to ensure that coarse grains were well mixed with the slurry rather than depositing at the bottom of the mixing tank.

We initiated flow using the lever system to release the restraint on the side-hinged headgate. This release, combined with the static force of debris flows bearing on the headgate and counterforce on the lever, caused it to swing open horizontally in about 0.5 s. The resulting flows began as nearly ideal dam-break flows and gradually accelerated during downstream propagation.

2.4 Decomposition of Impact Pressure Signals

The impact pressure signal of a debris flow is typically non-stationary and non-linear, and normally contains local fluctuations arising from different sources [e.g., *Hubl et al.,* 2009; *Cui et al.,* 2015]. With EMD, this complicated signal can be adaptively decomposed into a sum of a finite number of zero mean oscillating components termed Intrinsic Mode Functions (IMFs) without a priori basis function selection [*Huang et al.,* 1998]. EMD is based on the sequential extraction of energy

with intrinsic time scales of the signal from high to low frequencies [*Maheshwari and Kumar,* 2014]. A physically meaningful characterization of the signal can be obtained. Here, the EMD method is employed to decompose each impact pressure signal into a stationary mean pressure with a lower frequency and local fluctuations with higher frequencies (Figure 4). We first decomposed the impact pressure signal p_0 during the entire sampling process into IMFs and a residual r sequentially from high to low frequencies:

$$
\begin{aligned}
p_0(t) &= \text{IMF}_1(t) + \text{IMF}_2(t) + ... + \text{IMF}_n(t) + r(t) \\
&= \sum_{i=1}^{n} \text{IMF}_i(t) + r(t)
\end{aligned}
\tag{3}
$$

where IMF_i is the ith IMF and n is the total number of IMF components. A detailed description of the EMD decomposition process is provided in the supplementary document. The overall frequency spectra of the IMFs and the residual including their frequency band and amplitude during the entire process were obtained by the fast Fourier transform (FFT). An IMF is defined as a function that meets two conditions: (1) the number of zero-crossings and extremes must either be the same or differ at most by one, and (2) the envelopes defined by the local maxima and minima should be symmetric [*Huang et al.,* 1998]. The residual r does not need to satisfy the requirements of an IMF and takes the form of a function or a constant value. Then, impact pressure signals at different stages, delineated from a signal curve (before flow release, during flow release, during flow impact and after flow impact), are decomposed with EMD. The respective frequency spectra of the IMFs and the residual at different stages were obtained. The signal sources of the IMFs with

14

different frequencies were distinguished by comparing frequency spectra in these four stages.

EMD and FFT are invoked twice during the processing of impact pressure. On the first occasion, the overall frequency spectra of the IMFs and residual during the test are obtained. On the second occasion, the frequency spectra of the IMFs and residual at different stages are obtained to discriminate the signal sources of the IMFs and residual in the time domain. The power spectral density (PSD) of the impact pressure at different stages was obtained by the FFT:

$$P = \lim_{T \to \infty} \frac{1}{T} \int_{-T/2}^{T/2} \left(\sum_{i=1}^{n} \mathrm{IMF}_i(t) + r(t) \right)^2 dt = \frac{1}{2\pi} \int_{-\infty}^{\infty} \lim_{T \to \infty} \frac{|F_T(\omega)|^2}{T} d\omega \tag{4}$$

$$\mathrm{PSD} = \lim_{T \to \infty} \frac{|F_T(\omega)|^2}{2\pi T} \tag{5}$$

where $\omega = 2\pi f$ is the angular frequency and f is the frequency. For the released flows in our experiments, eight IMF components are sufficient to describe the impact pressure signals. This is because the main frequency of IMF_8 is lower than 0.5 Hz, which is 0.025% of the sampling frequency.
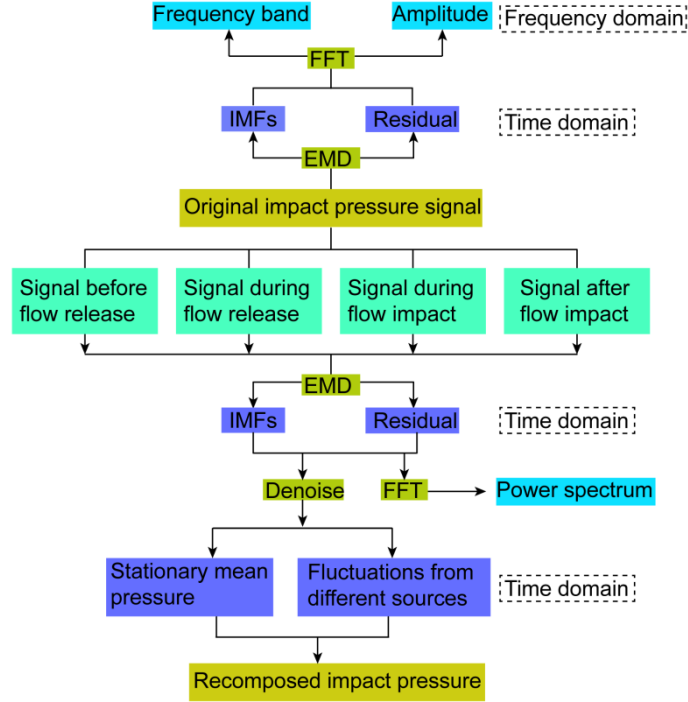
Figure 4. Analysis procedure for the impact pressure signals. The signal before flow release is used to observe the noise in the system.

2.5 Dimensionless Characterization of Flow Regimes

The flow regimes for debris flows are characterized according to the stresses that govern their motion [*Iverson,* 1997; *Savage and Hutter,* 1989]. The Bagnold number $N_{Bag} = \dfrac{C_v \rho_g \gamma d_s^2}{(1 - C_v)\eta}$ defines the relative dominance between collisional and viscous forces, where γ is the flow shear rate ($\gamma = \dfrac{v}{h}$). The Savage number $N_{Sav} = \dfrac{\rho_g d_s^2 \gamma^2}{(\rho_g - \rho_s)gh \tan\varphi}$ is the ratio between collisional and frictional forces where φ is the internal friction angle and g is the acceleration due to gravity. The friction number $N_{Fri} = \dfrac{C_v (\rho_g - \rho_s)gh \tan\varphi}{(1 - C_v)\gamma\eta}$ is the ratio between frictional and viscous forces.

The grain Reynolds number $N_{Rg} = \dfrac{\rho_s \gamma d_s^2}{\eta}$ is the ratio between the solid inertial stress

and the fluid viscous shearing stress.

These dimensionless numbers are typically used to classify the dominant energy dissipation mechanisms in natural [*Iverson,* 1997] and experimental [*de Haas et al.,* 2015] debris flows. Collisional forces dominate over viscous forces when $N_{Bag} > 200$; collisional forces dominate over frictional forces when $N_{Sav} > 0.1$ [*Bagnold,* 1954; *Savage and Hutter,* 1989]. When $N_{Fri} > 250$, frictional forces dominate over viscous forces [*Parsons et al.,* 2001; *de Haas et al.,* 2015]. Generally, debris flows begin to show inertial effects and deviate significantly from ideal viscous behavior when $N_{Rg} > 1$ [*Vanoni,* 1975].

3. Results and Analysis

In this section, we first describe the general characteristics of the experimental debris flows. Then we discuss the flow regimes of the debris flows with various volume concentrations in terms of their dimensionless numbers. Next, we identify the components of impact pressure signals. Finally, we assess the effects of flow regime and volume concentration on the impact pressures.

3.1 General Flow Characteristics

Following opening of the headgate, a flow quickly initiated as a result of the dam-break initial condition and strong longitudinal thrust imparted by subsequent flow. The released flows with slurry density $\rho_s = 1000–1300$ kg/m^3 flowed turbulently downwards. By contrast, for released flows with $\rho_s = 1350$ kg/m^3 flow behavior was

similar to a plug flow in the depth direction due to the high viscosity (Figure S3). The coarse grains (5–8 mm), shown in brown on Figure 5, segregated upwards to the surface of a debris flow with a low slurry density and were then preferentially transported to the front by the bulk flow, where they could be overrun, recirculated, and accumulated. However, no segregation of coarse grains was observed for debris flows with ρ_s = 1350 kg/m^3. Each agitated flow impacted the steel plate mounted to the pressure sensor and was fully diverted upwards (Figure S4), producing a jet-like flow at the flume exit due to a high Froude number representing the relative effects between flow inertia and gravity.
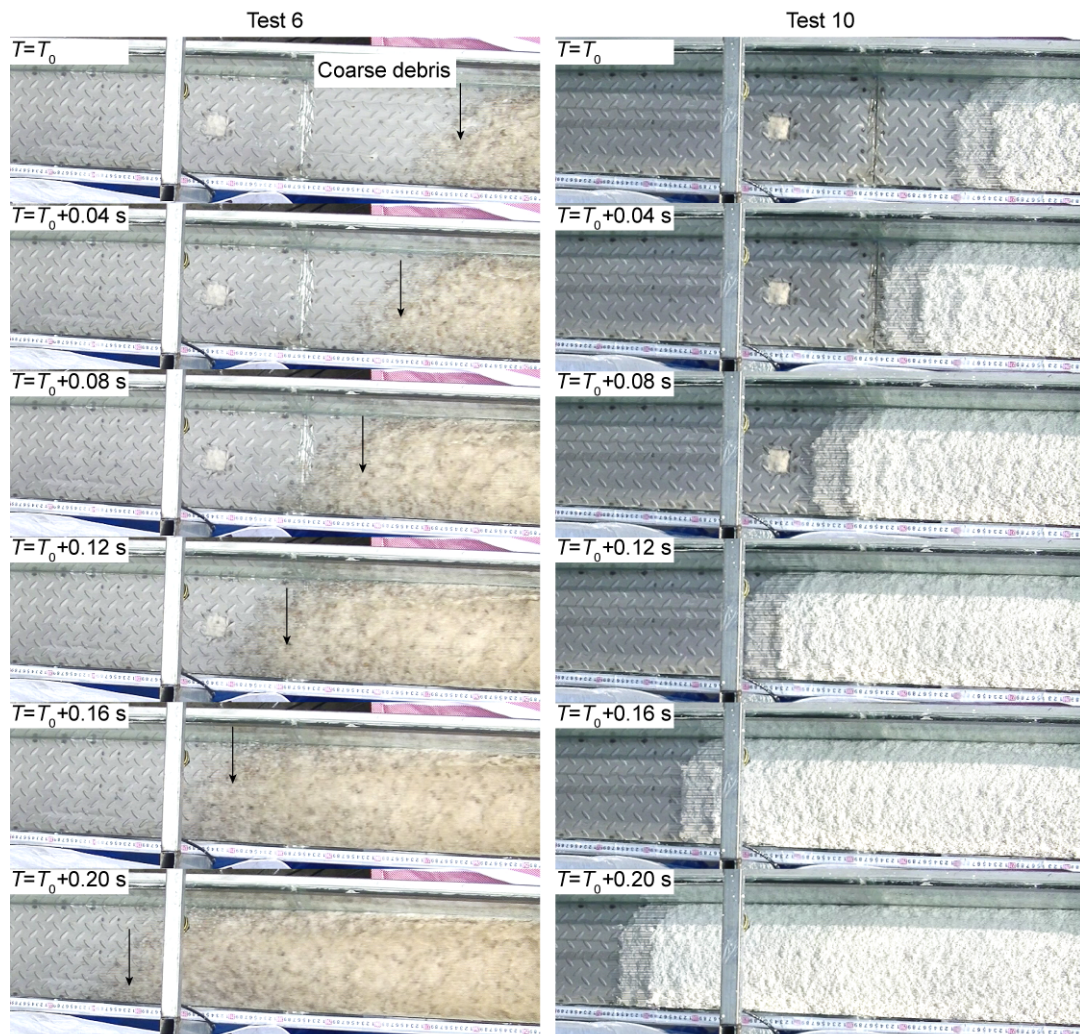
Figure 5. Top view of the propagation process of debris flows in tests 6 and 10. Significant segregation of coarse grains (5–8 mm) in brown, indicated by black arrows, was observed in test 6 but not in test 10. T_0 is the time corresponding to the first frame.

The flow-front velocity at the flume exit in the experimental runs was between 2.85 m/s and 4.90 m/s (Figure 6 and Table S1). The flow-front velocity first increased with increasing slurry density but decreased when ρ_s exceeded 1200 kg/m^3. The flow-front velocity decreased with increasing debris-grain concentration. The flow-front depth at the flume exit was in the range 0.05–0.07 m. It generally decreased with increasing slurry density and did not show a significant dependence on the debris-grain concentration.
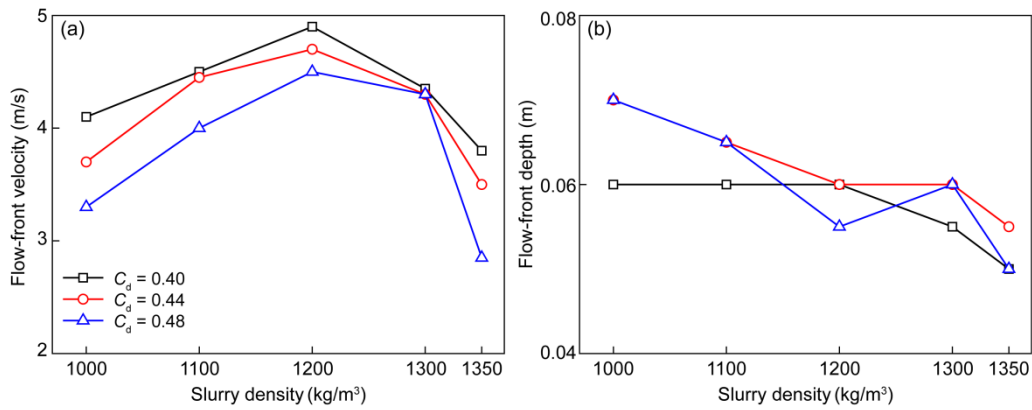

Figure 6. Flow-front velocity (a) and depth (b) of debris flows at the flume exit.

3.2 Flow Regimes

Debris flows transition from collisional to viscous flow regimes and from frictional to viscous flow regimes with increasing slurry density (Figures 7a–7c). By contrast, the effect of debris-grain concentration on the flow regime is minor.

Collisional forces dominate over viscous forces when ρ_s = 1000–1100 kg/m^3 and a reverse tendency occurs when ρ_s = 1100–1350 kg/m^3 (Figure 7a). Collisional forces were dominated by frictional forces for each debris flow presented in Figure 7b. Frictional forces dominate over viscous forces when ρ_s = 1000–1200 kg/m^3 while flows present primarily viscous behavior when ρ_s = 1300 kg/m^3 and 1350 kg/m^3 (Figure 7c). Grain interactions become more effectively buffered as the slurry viscosity in the pores increases because the fluid inertia increasingly outweighs the grain inertia (Figure 7d).
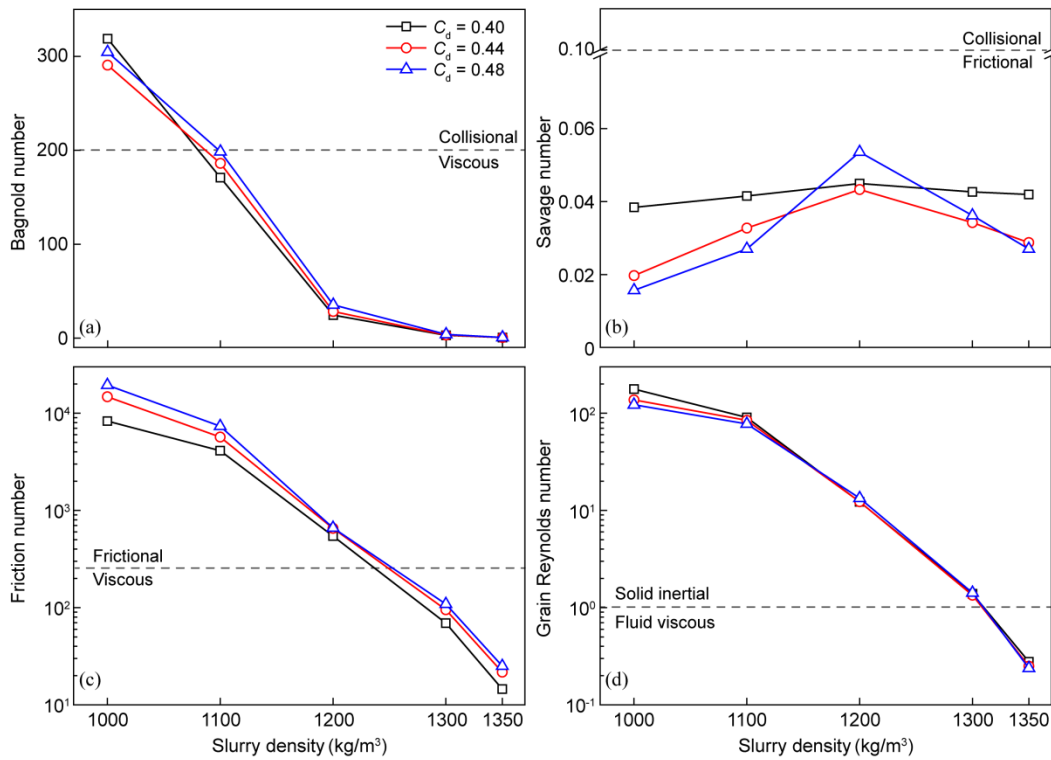

Figure 7. Effects of slurry density and debris-grain concentration on the flow regime: (a) Bagnold number; (b) Savage number; (c) friction number; (d) grain Reynolds number.

3.3 Features of Impact Pressure Spectra

The impact pressure spectra of released slurries and debris flows at different stages were analyzed based on the comparisons between tests 1 and 6 and between tests 2 and 7 (Figures 8 and 9, respectively). The respective densities of pure slurries in tests 1 and 2 are 1000 kg/m^3 and 1100 kg/m^3, which are identical to those of the debris flows in tests 6 and 7 with C_d = 0.40. The decomposition process of impact pressure signals is shown in Figures S5–S6. The comparisons of impact pressure spectra between pure slurries and debris flows with the same slurry density are similar for other tests.

For clear water in test 1, sampling noise from the data collecting instrument with main frequencies of 50 Hz, 150 Hz, 250 Hz and 350 Hz was detected before flows were released (Figure 8b). Resonance of the experimental apparatus at a main frequency around 300 Hz occurred when the headgate was opened (Figure 8c). The resonance intensity gradually attenuated as the flow passed through the flume channel. The sampling noise and resonance of the experimental apparatus were eliminated from the measured signal to enable a precise analysis of the impact pressure induced by the released flows. When the bulk flow reached the pressure sensor at the flume exit, a stationary mean pressure (SMP) was developed which resulted in a frequency smaller than 20 Hz on the spectra (Figure 8d). After the entire flow went through the flume exit, only sampling noise remained.

Compared with the pure slurries, a significant fluctuating pressure (FP) with a frequency 800–1000 Hz occurred for debris flows including debris grains during the

impact process (Figures 8h and 9h). The FP at the flow front is much stronger than that at the flow body (Figures S5 and S6). The local fluctuations for the debris flow in test 7 appeared when coarse debris grains that had segregated from the bulk flow impacted the sensor prior to bulk flow (Figure S7). At a time of 0.08 seconds later, the bulk flow reached the sensor, generating an impact pressure consisting of a SMP and a FP. On this basis, it is inferred that the FP arose from the collision of coarse grains. It is consistent with the physical model proposed by *Farin et al.* [2019] that a high-frequency seismic signal is generated by the collision of coarse grains. The PSD of the SMP is several orders of magnitude higher than that of the FP due to a long-lasting flow pressure.
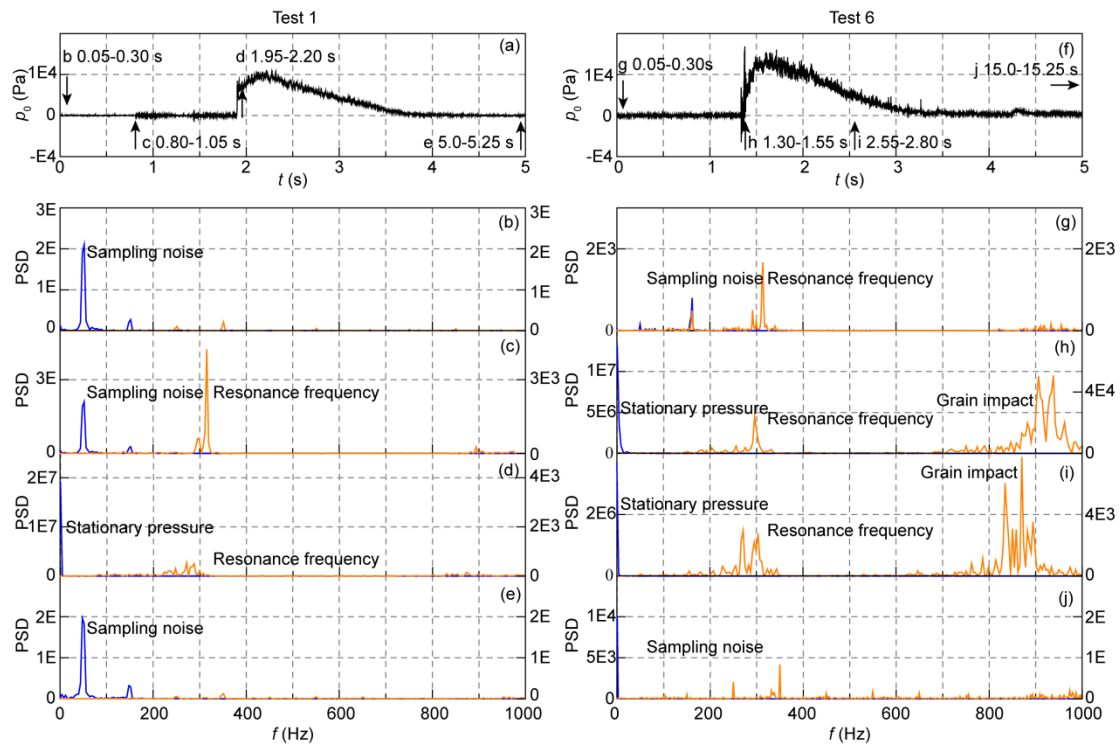

Figure 8. Power spectral densities (PSDs) of impact pressure signals at different stages of tests 1 and 6. The orange lines denote the PSDs of IMF_1 and IMF_2, while the blue lines denote the PSDs of IMF_3–IMF_8 and the residual for each test. Figures (b),

(c), (d) and (e) display the PSDs of pure slurry in test 1 at different stages in Figure (a). Similarly, Figures (g), (h), (i) and (j) display the PSDs of debris flow in test 6 at different stages in Figure (f). The resonance of the experimental apparatus in test 6 prior to flow release was due to the vibration of the blenders.
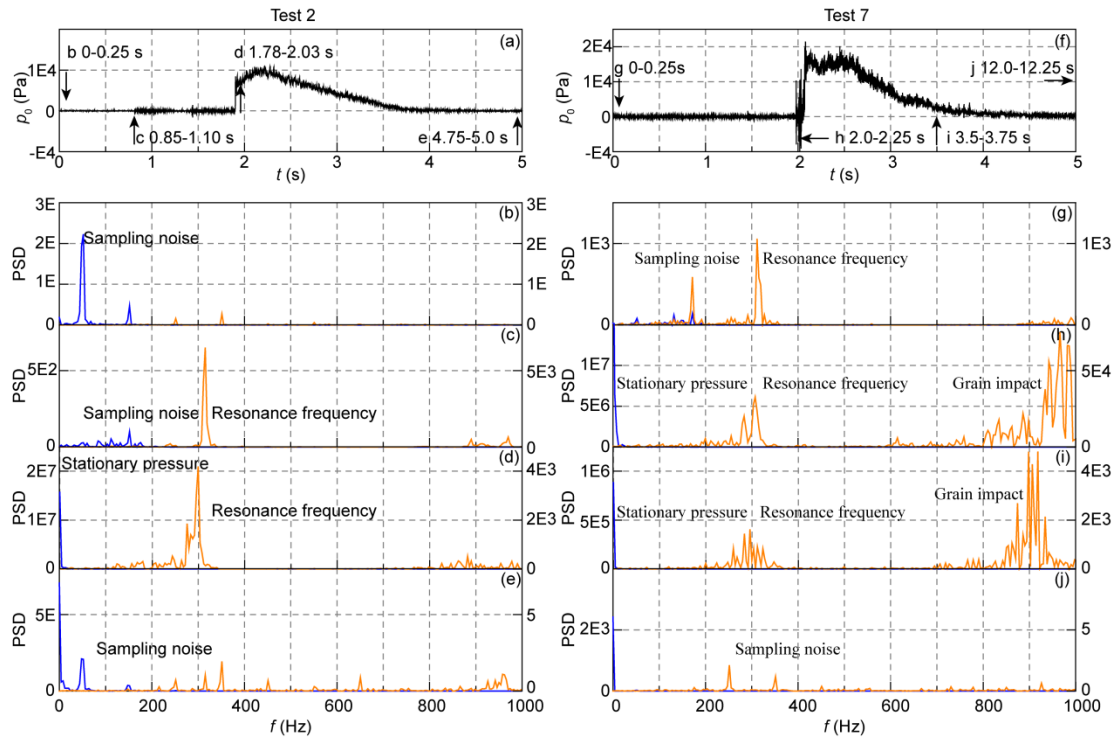

Figure 9. PSDs of impact pressure signals at different stages of tests 2 and 7.

The impact pressure p_b of each debris flow was recomposed from the bulk-flow induced SMP (main frequency < 20 Hz) and the FP (800–1000 Hz) from the hard impact of coarse grains without considering the sampling noise, environmental noise and resonance frequency (Figures 10 and S8). Only small deviations are observed between the measured impact pressure p_0 and recomposed impact pressure p_b, displaying a high signal-to-noise ratio. The peak FPs of all debris flows appeared before the respective peak SMPs were reached. The peak impact pressure p_{bm} coincided with the peak FP (test 6) or with the peak SMP (all other tests).
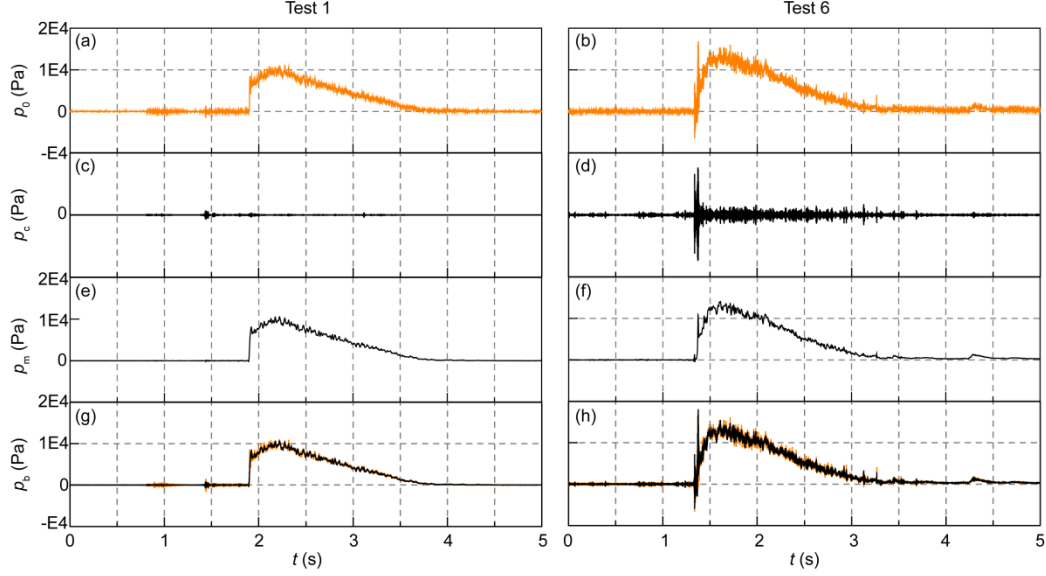
Figure 10. Recomposition of impact pressures with the SMP and FP in tests 1 and 6: (a) and (b) impact pressure signal p_0; (c) and (d) fluctuating pressure p_c from the hard impact of coarse grains; (e) and (f) stationary mean pressure p_m; (g) and (h) recomposed impact pressure p_b.

3.4 Stationary Mean Pressures from the Bulk Flow

Inertia prevails over gravity for each flow during the impact process due to a high Froude number F_r (larger than 4.2, as shown in Table S1), contributing to the formation of an upward jet. An analytical model (jet model) for flow impact against an obstacle is established using the Bernoulli equation to predict peak SMP p_{mm} (Figure S9).

$$z_1 + \frac{p_1}{\rho_b g} + \frac{\alpha_1 v_1^2}{2g} = z_2 + \frac{p_2}{\rho_b g} + \frac{\alpha_2 v_2^2}{2g} \tag{6}$$

where z_1, p_1, v_1 represent the height above the reference plane, pressure and mean flow velocity at the incident flow front and z_2, p_2, v_2 represent the corresponding values at the top of the jet flow. The energy loss caused by turbulent and viscous

24

stress is not calculated in Equation (6) considering the incident flow front is close to the jet flow. α is the correction coefficient of flow kinetic energy. α is taken as 1.0 for the released slurries and debris flows in our experiments as a result of a large F_r [*Song et al.,* 2021]. Assuming a hydrostatic pressure distribution in the depth direction, the mean impact pressure p_w exerted on the steel panel is found to be

$$p_\mathrm{w} = p_1\left(1+0.5\alpha_1 F_r^2\right) - \rho_b g h_o \tag{7}$$

where h_o is the vertical distance from the panel center to the flume bottom. A detailed derivation is provided in the supplementary document.

As shown in Figure 11, the impact pressures p_w calculated by the jet model accurately predict the peak SMP p_mm measured from the impact tests of all slurries and debris flows. This indicates that the jet model based on the Bernoulli equation is able to calculate the impact pressure caused by fluid-phase flow thrusting.

We find a clear maximum in the relations between the peak SMP and the slurry density. p_mm and p_w firstly increase with increasing slurry density and then decrease when ρ_s is larger than 1200 kg/m^3, regardless of debris-grain concentration. The bulk density of the released flow increases with increasing slurry density and thus the impact pressure increases with increasing hydrostatic pressure of the incident flow (Equation (7)). On the other hand, debris flows with $\rho_\mathrm{s} = 1000\text{–}1200$ kg/m^3 are within the frictional flow regime (Figure 7). The liquefaction ratio of debris flow increases with increasing slurry density (Table S1). This is because denser slurries have a higher viscosity (Figure 2a) and lower diffusion coefficient of pore-fluid pressure [*de Haas et al.,* 2015]. The effective stress and the corresponding basal shear stress of debris

flows are significantly reduced by the nonequilibrium pore-fluid pressure caused by the increase of slurry density (Figure 12). The mean flow-front velocity is enhanced because of the low basal shear resistance (Figure 6), resulting in increased impact pressures. By contrast, debris flows transition into the viscous flow regime when $\rho_s >$ 1200 kg/m^3. The mean flow-front velocity is reduced by the enhanced viscous resistance (Figure 6) and thus impact pressures of debris flows decrease.

The impact pressures of debris flows generally decrease with the increase of debris-grain concentration except for $\rho_s = 1300$ kg/m^3 (Table S1). The basal frictional resistance increases with the increase of debris-grain concentration for $\rho_s = 1000–$ 1200 kg/m^3 and significant viscous resistance tends to retard the motion of debris grains for $\rho_s = 1350$ kg/m^3, reducing the mean flow-front velocity and impact pressure. By contrast, liquefaction ratios of debris flows are larger than 0.73 and viscous resistance is relatively limited for debris flows with $\rho_s = 1300$ kg/m^3. The mean flow-front velocity slightly decreases with the debris-grain concentration for $\rho_s =$ 1300 kg/m^3 due to the low shear resistance (Figure 6). The increase in impact pressures of debris flows is attributed to the increase of bulk density and hydrostatic pressure of the incident flow (Equation (7)).
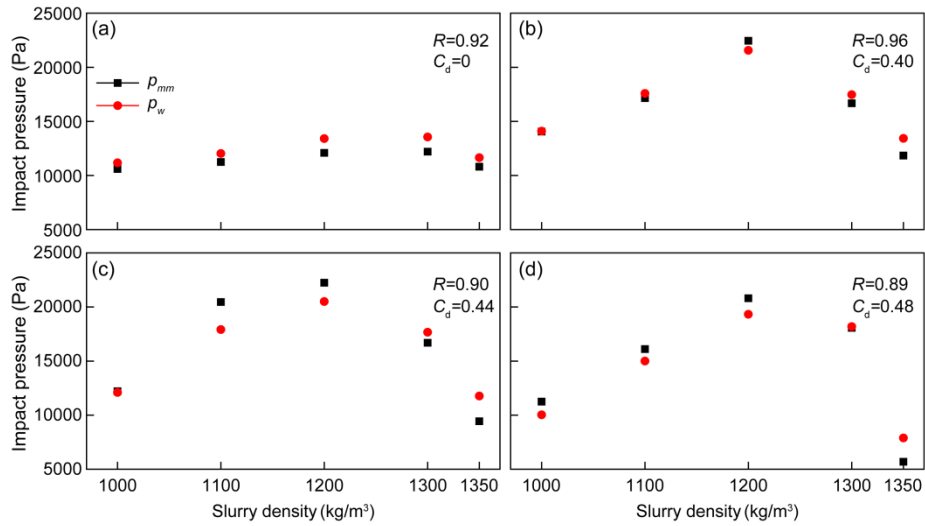
Figure 11. Comparison between the maximum SMP measured from impact tests, p_{mm}, and the impact pressure calculated from the analytical model, p_w: (a) pure slurries in tests 1–5; (b) debris flows in tests 6–10; (c) debris flows in tests 11–15; (d) debris flows in tests 16–20.
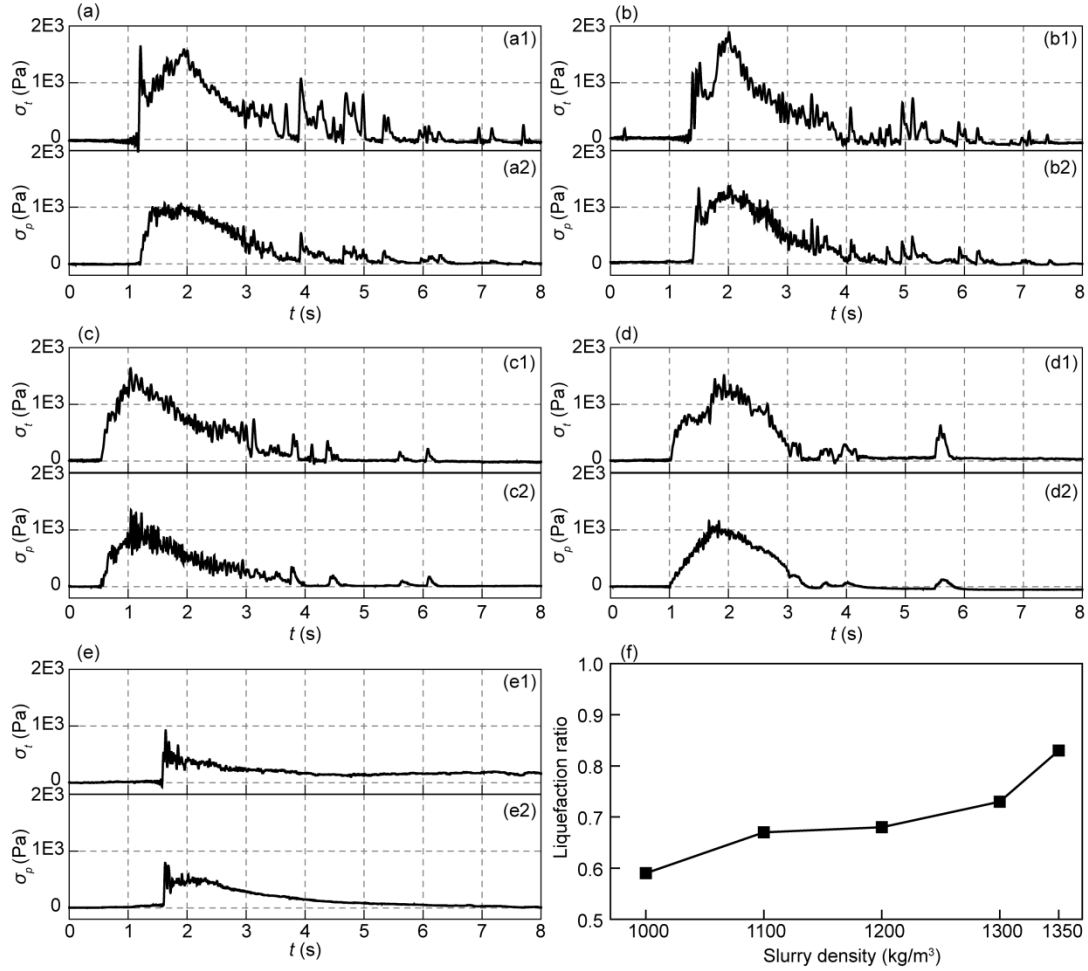
Figure 12. Measurements of basal total normal stress, σ_t (t), and basal pore pressure, σ_p (t), at x = 3.2 m (a–e) and liquefaction ratio (f) in tests 6–10. Filtering is adopted to eliminate fluctuations of σ_t (t) and σ_p (t). After debris flow passes over the pore-pressure sensor, part of the debris flows in tests 10, 15 and 20 is deposited on the bottom of the flume due to viscous slurry and thus σ_t (t) and σ_p (t) are greater than 0.

3.5 Fluctuating Pressure from Collisions of Coarse Grains

Compared with the SMPs, the PSDs of FPs were relatively low due to the short duration of grain collisions. However, the peak fluctuating pressure p_{cm} was more than 20% of p_{mm} for all debris flows presented here (Table S1). Its significance makes it necessary to take the FP into account when predicting the impact pressure of debris

28

flows.

The fluctuating pressure p_g from the collision of coarse grains can be derived based on the impulse–momentum theorem [e.g., *Bugnion et al., 2012; Scheidl et al., 2013*]:

$$p_g = \beta \rho_c v^2 \tag{8}$$

where the degree of segregation of coarse grains β quantifies the accumulation of coarse grains at the flow front [*Zhou et al., 2020*]. β is calculated from the fluctuating pressure p_g and flow-front velocity v. As shown in Figure 13(a), the measured p_{cm} are well represented by the quadratic velocity-dependent formula by assuming a degree of segregation of coarse grains β = 2.0, 1.2 and 1.1 for C_d = 0.40, 0.44 and 0.48. The fluctuating pressures p_{cm} and p_g increase first with increasing slurry density and then decrease when ρ_s is larger than 1200 kg/m^3, regardless of debris-grain concentration (Figure 13(b)). The variation of the FP with slurry density has a consistent trend with that of the SMP.
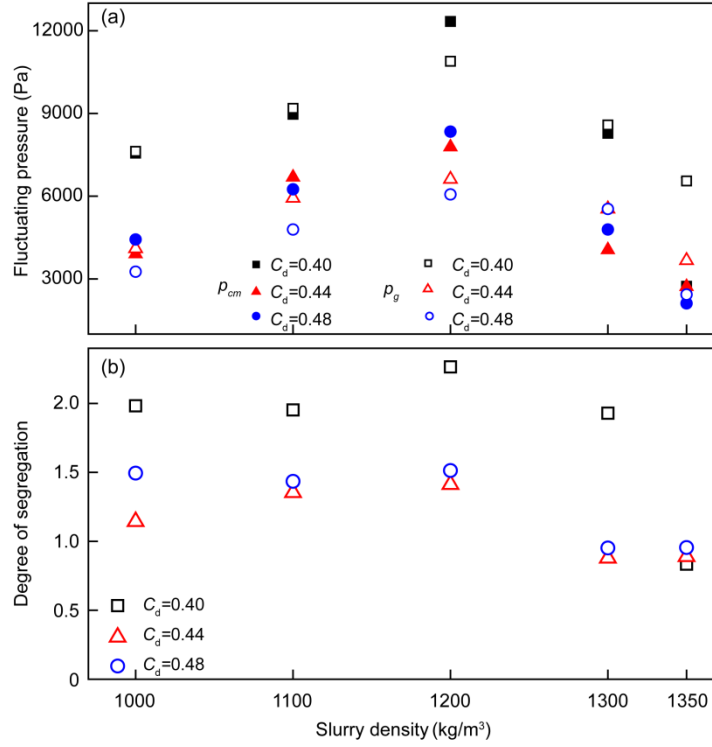
Figure 13. (a) Comparison between the maximum fluctuating pressure measured from impact tests, p_{cm}, and the collision pressure calculated from the impulse–momentum theorem, p_g, assuming a degree of segregation of coarse grains $\beta = 2.0$, 1.2 and 1.1 for $C_d = 0.40$, 0.44 and 0.48. (b) The back-calculated β based on Equation (8) in each test.

The back-calculated β based on Equation (8) is in the range 0.8–2.2 in the experimental runs. Particle size segregation occurs in debris flows when small particles preferentially fall down into randomly occurring voids beneath them while large particles move up to the free surface [*Vallance and Savage,* 2000]. This process can be explained by gravity-induced and shear-gradient-induced segregation mechanisms [*Weinhart et al.,* 2013; *Hill and Tan,* 2014]. For the former, the contact stress gradient of coarse grains is higher than that of fine grains. For the latter, coarse grains are segregated to the free surface in the region of low kinetic stress. The

gradients of contact stress and kinetic stress can effectively push the coarse grains upwards [*Staron and Phillips,* 2015].

On this basis, we attempt an interpretation of the tendency of coarse grains to segregate with slurry density (Figure 13b). A simplified model of segregation rate q proposed by *May et al.* [2010] is expressed as

$$q = s_r \dot{\gamma} \tag{9}$$

where s_r is a non-dimensional segregation number which is directly proportional to the reduced gravitational acceleration $g' = (\rho_g - \rho_s) g / \rho_g$ due to buoyancy [*Gray and Thornton,* 2005; *Zhou et al.,* 2020]. The flow velocity and shear rate of the debris flows presented here increase with slurry density when $\rho_s < 1200$ kg/m³. The kinetic stress gradient is enhanced by the increased flow shear rate [*Staron and Phillips,* 2015]. On the contrary, the contact stress gradient of coarse grains is reduced due to the increase in the buoyancy of ambient slurry [*Zhou et al.,* 2020]. Accordingly, the degree of segregation of coarse grains initially increases slightly with slurry density due to the dual control of slurry buoyancy and shear rate (Equation (9)). By contrast, a rapid decrease of the degree of segregation of coarse grains occurs for $\rho_s > 1200$ kg/m³. Fluid drag stresses become significantly enhanced in viscous flows considering slurry viscosities at $\rho_s = 1300$ kg/m³ and 1350 kg/m³ exceed those at $\rho_s = 1000$ kg/m³ and 1100 kg/m³ by two orders of magnitude (Figure 2a). The contact stress gradient in viscous flow is significantly counteracted by the buoyancy and fluid drag stresses of ambient slurry with high density. Moreover, viscous stresses induce the formation of nearly plug flows in tests 10, 15 and 20 (Figure S3) wherein local

shear rates are reduced; the segregation of coarse grains is thus significantly inhibited.

4. Discussion

4.1 Characteristics of the Fluctuating Pressure

Peak FPs appear before peak SMPs due to the fast transport of coarse grains at the flow front (Figures S5 and S6). Subsequently, the FP rapidly attenuates because a significant local dynamic fluid pressure develops near the steel panel during the impact process (Figure 14). The resulting dynamic fluid-pressure gradient tends to retard the impact of the debris grains on the steel panel due to the increased fluid drag forces on the solid phase. This interacting process is revealed by *Levy and Sayed* [2008] using a two-phase flow model. Finally, the measured impact pressure of debris flow gradually declines to the dynamic fluid pressure at the rear of the debris flow with finer-grained, more dilute and liquefied materials.
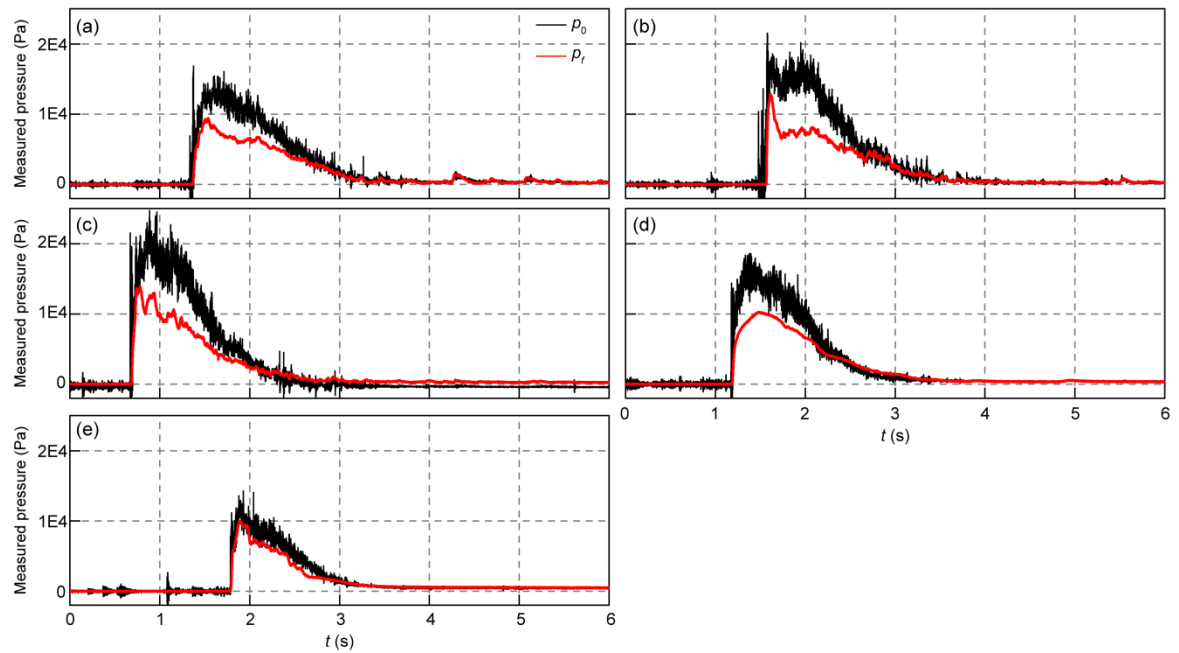

Figure 14. Measured impact pressure, p_0 (t), and dynamic fluid pressure, p_f (t), at the

flume exit (a–e) in tests 6–10.

The FPs in our experiments are analogous to seismic vibrations induced by debris flows where significant ground velocities and normal-stress fluctuations are caused by coarse-grain collisions [*Farin et al.,* 2019; *de Haas et al.,* 2021]. Strong normal-stress fluctuations with a high frequency occur at the flow front and rapidly decrease at the flow body as a result of grain segregation [*de Haas et al.,* 2021]. In addition, the seismic vibrations of debris flows are also enhanced by the concentration of coarse grains and suppressed by the slurry density.

Flow velocity has a vital influence on the FP and SMP of a debris flow indicated by Equations (7) and (8). The effect of the depth of the incident flow on the FP and SMP is secondary. However, runup of debris flows against obstacles is closely related to the depth of incident flow [*Iverson et al.,* 2016]. The peak FP is more than half of the peak SMP in tests 6–8. The peak FP for a natural debris flow can be enhanced when flow-front velocity is higher than the measured values in this study. Hence, it is of importance to take the FP into account when predicting the impact pressure of debris flows.

4.2 Impact Coefficient of the Hydrodynamic Formula

The peak impact pressure p_{bm} recomposed from the SMP and the FP can be described by the hydrodynamic formula (Equation (2)). The calculated λ is in the range 0.4–0.7 in our experiments (Figure 15) and consistent with reported values (0.4–0.8) for hillslope debris flows in Veltheim [*Bugnion et al.,* 2012] and the values (0.3–0.7) for the debris flows in British Columbia [*Hungr et al.,* 1984] and Jiangjia
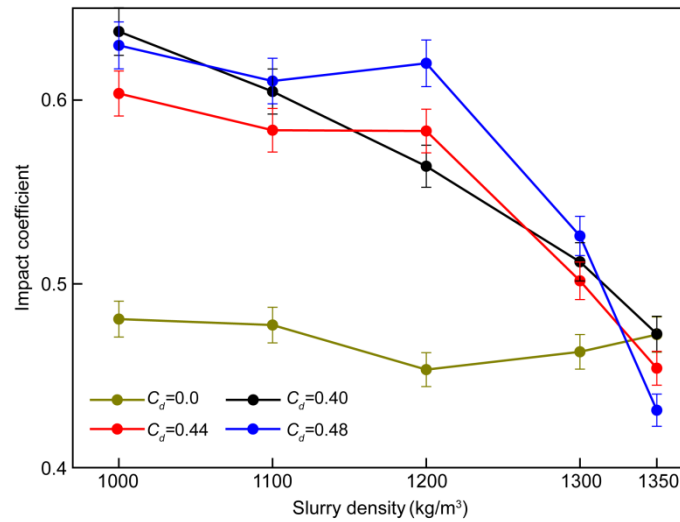
Ravine [*Hu et al., 2011*].

Figure 15. Impact coefficient λ for the experimental debris flows presented here. The error bars for λ are inferred from the errors in flow-front velocity.

The impact coefficient generally decreases with the increase of slurry density for all released flows. The impact coefficients of pure slurries are smaller than those of debris flows with the same slurry density and the difference between these two sets of impact coefficients gradually narrows with the increase of slurry density (Figure 15). The effect of intergranular stresses including frictional and collisional stresses relative to viscous stresses becomes weakened with increasing slurry density due to increases in the viscosity of slurry and liquefaction ratio of debris flow [*Kaitna et al., 2016*]. The impact pressure produced by the collision of debris grains is suppressed by the ambient slurry, resulting in a decrease in the impact coefficient. The measured dynamic fluid pressures approximate the corresponding impact pressures in tests 10, 15 and 20 (Figure 14), indicating that debris flows display prominent fluid viscous rather than grain inertia (Figure 7d).

The impact coefficients measured from debris flows in some model experiments

and in the field can be larger than unity [*Watanabe and Ikeya,* 1981; *Scheidl et al.,* 2013; *Cui et al.,* 2015]. The reason for the difference is because the sizes of coarse grains in the debris flow in those measurements are similar in magnitude to the panel which bears the impact pressure. A point-wise loading is induced by each coarse grain collision [*Scheidl et al.,* 2013], causing a stress concentration on the panel. The magnitude of point impact depends on the kinetic energy, diameter of coarse grains and contact deformation which can be estimated using the Hertz model [*Hungr et al.,* 1984]. The amplitude of point-wise impact significantly decreases as the panel size is increased [*Iverson,* 1997; *Bugnion et al.,* 2012]. The effect of point-wise loading on the impact pressure is negligible in our experiments because the panel size is more than ten times the diameter of the coarse grains.

4.3 Segregation of Coarse Grains

The degree of segregation of coarse grains in all tests is less than 2.2 because of a short migration distance (4.0 m). For a natural debris flow, the segregation of coarse grains can be more pronounced due to migration distances of several kilometers or even tens of kilometers [*Iverson,* 1997; *de Haas et al.,* 2018].

Our experiments show that the buoyancy of the ambient slurry has a negative effect on the grain segregation in debris flows. These results are consistent with experiments conducted using chute flows [*Vallance and Savage,* 2000; *Zanuttigh and Ghilardi,* 2010; *De Haas et al.,* 2015] and simulations of grain segregation in flows with different interstitial fluid [*Pudasaini and Fischer,* 2020; *Zhou et al.,* 2020]. This is because the contact stress gradient of debris grains is counteracted by the buoyancy

of ambient slurry. The grain segregation is sensitive to the shear rate of debris flow, which is in accord with numerical observations [*Staron and Phillips,* 2015; *Itoh and Hatano,* 2019].

More importantly, our results show that grain segregation diminishes as the fluid viscosity increases but intensifies when the viscosity is below a certain threshold value (i.e., 0.015 Pa s). The transition in the dependence of grain segregation on viscosity coincides with the transition of the flow rheology from being dominated by viscous or frictional stresses (Figure 7). This transition is consistent with the numerical simulation of grain segregation using computational fluid dynamics coupled with the discrete element method [*Cui et al.,* 2021]. In viscous flows, fluid drag stresses become relevant which weaken contact stress gradients necessary in driving coarse grains upward. In the frictional regime, the flow velocity and shear rate are enhanced by the nonequilibrium pore-fluid pressure (Figures 6 and 12), which in turn boost kinetic stress gradients and contribute to the segregation of coarse grains.

4.4 Implications

We have proposed a method to predict the stationary mean pressure and the fluctuating pressure of debris flows based on their physical properties. The predictive models of impact pressure are applicable to experimental debris flows with collisional, viscous or frictional flow regimes (Figure 7). This means that the predictive models are appropriate for natural debris flows with different regimes. Gravel with a diameter of 5–8 mm is the segregated debris at the flow front in this study. However, the diameter for grain segregation in natural debris flows with particles ranging from clay

to large boulders is still an open question [*Cui et al.,* 2021]. The impact pressures of debris flows exerted on structures can be estimated according to a certain weight coefficient for the combination of the stationary mean pressure and the fluctuating pressure, considering that these two pressures do not peak simultaneously (Figure 10).

The predictive models of impact pressure can be used for the designs of infrastructure and disaster-mitigation structures in mountainous regions. In addition, these models may be suitable for other geophysical flows composed of solid and fluid phases, like pyroclastic flows which are ground-hugging, dense, gas–particle mixtures generated during volcanic eruptions [*Roche et al.,* 2013].

5. Conclusions

We experimentally investigate the impact pressure characteristics of debris flows. In particular, the measured impact pressure signal is decomposed into a stationary mean pressure and local fluctuations from different sources through empirical mode decomposition. The main concluding remarks are:

(1) The impact pressure of each debris flow is decomposed into the stationary mean pressure with low frequency from the bulk flow and the fluctuating pressure with high frequency from the coarse debris grains. The peak stationary mean pressures are predicted well with the Bernoulli equation and the peak fluctuating pressures are efficiently described by the impulse–momentum theorem.

(2) The peak stationary mean pressures and fluctuating pressures first increase with increasing slurry density and then decrease. This is due to the dual control exerted by the basal frictional stress and viscous stress of debris flows.

(3) The transition in the dependence of grain segregation on viscosity coincides with the transition of the flow rheology from being dominated by viscous or frictional stresses. The impact coefficient of debris flows generally decreases with the increase of slurry density due to the local dynamic fluid pressure.

Data Availability Statement

For each test, the measured impact pressure signal, dynamic fluid pressure at the flume exit, basal total normal stress and pore pressure at $x = 3.2$ m are available at https://doi.org/10.5281/zenodo.5148243.

Notation

C_d volume concentration of debris grains

C_v volume concentration of a debris flow

d_s mean particle diameter

f frequency

F_r Froude number

g gravitational acceleration

h flow-front height

h_0 vertical distance from the panel center to the flume bottom

i hydraulic gradient

IMF_i the ith intrinsic mode function

k empirical factor for hydrostatic model

N_{Bag} Bagnold number of debris flow

N_{Fri} friction number of debris flow

N_{Rg} grain Reynolds number of debris flow

N_{Sav} Savage number of debris flow

p_0 measured impact pressure of a flow

p_1 pressure at the incident flow front

p_2 pressure at the top of the jet flow

p_b recomposed impact pressure of a flow

p_c fluctuating pressure for coarse grains

p_{bm} peak impact pressure of a flow without noise

p_{cm} peak fluctuating pressure

p_{mm} peak stationary mean pressure of a flow

p_{peak} peak debris-flow impact pressure

p_w impact pressure exerted on the steel panel

q segregation rate of coarse grains

r residual

R^2	determination coefficient
s_r	non-dimensional segregation number
v	flow-front velocity
v_1	flow velocity at the incident flow front
v_2	flow velocity at the top of the jet flow
V_0	volume of released flow
z_1	height above the reference plane at the incident flow front
z_2	height above the reference plane at the top of the jet flow
α	correction coefficient of flow kinetic energy
β	degree of segregation of coarse grains
θ	slope angle of the flume
ρ_b	bulk density of a debris flow
ρ_c	dry density of coarse grains
ρ_d	dry density of debris grains
ρ_g	solid particle density
ρ_s	slurry density
ρ_w	water density
σ_p	basal pore pressure
σ_t	basal total normal stress
η	dynamic viscosity of a slurry
γ	flow shear rate
λ	impact coefficient of released flow

ω angular frequency

φ internal friction angle of debris grains

References

Bagnold, R. A. (1954), Experiments on a gravity-free dispersion of large solid spheres in a Newtonian fluid under shear, *Proc. R. Soc. A, 225*(1160), 49–63.

Bugnion, L., B. W. McArdell, P. Bartelt, and C. Wendeler (2012), Measurements of hillslope debris flow impact pressure on obstacles, *Landslides, 9(2),* 179–187.

Costa, J. E. (1988), Rheologic, geomorphic, and sedimentologic differentiation of water flood, hyperconcentrated flows, and debris flows, in *Flood Geomorphology*, chap. Rheologic, geomorphic, and sedimentologic differentiation of water floods, hyperconcentrated flows, and debris flows, pp. 113–122, John Wiley, New York.

Cui, K. F. E., G. G. D. Zhou, and L. Jing (2021), Viscous effects on the particle size segregation in geophysical mass flows: Insights from immersed granular shear flow simulations, *J. Geophys. Res.-Solid Earth, 126,* e2021JB022274.

Cui, P., C. Zeng, and Y. Lei (2015), Experimental analysis on the impact force of viscous debris flow, *Earth Surf. Process. Landf., 40(12),* 1644–1655.

de Haas, T., A. L. Densmore, M. Stoffel, H. Suwa, F. Imaizumi, J. A. Ballesteros-Cánovas, and T. Wasklewicz (2018), Avulsions and the spatio-temporal evolution of debris-flow fans, Earth-Sci. Rev., 177, 53–75.

de Haas, T., L. Braat, J. R. F. W. Leuven, I. R. Lokhorst, and M. G. Kleinhans (2015), Effects of debris flow composition on runout, depositional mechanisms, and deposit morphology in laboratory experiments, *J. Geophys. Res.-Earth Surf., 120,* 1949–1972.

de Haas, T., A. S. Åberg, F. Walter, and Z. Zhang (2021), Deciphering seismic and normal-force fluctuation signatures of debris flows: an experimental assessment of

effects of flow composition and dynamics, *Earth Surf. Process. Landf.,* 1–14. DOI: 10.1002/esp.5168.

Farin, M., V. C. Tsai, M. P. Lamb, and K. E. Allstadt (2019), A physical model of the high-frequency seismic signal generated by debris flows, *Earth Surf. Process. Landf., 44(13),* 2529–2543.

Gray, J. M. N. T., and A. R. Thornton (2005), A theory for particle size segregation in shallow granular free-surface flows, *Proc. R. Soc. A, 461,* 1447–1473.

Gray, J. M. N. T., and P. Kokelaar (2010), Large particle segregation, transport and accumulation in granular free-surface flows, *J. Fluid Mech., 652,* 105–137.

Hill, K. M., and D. S. Tan (2014), Segregation in dense sheared flows: Gravity, temperature gradients, and stress partitioning, *J. Fluid Mech., 756,* 54–88.

Hsu, L., W. E. Dietrich, and L. S. Sklar (2014), Mean and fluctuating basal forces generated by granular flows: Laboratory observations in a large vertically rotating drum, *J. Geophys. Res.-Earth Surf., 119*(6), 1283–1309.

Hu, K., F. Wei, and Y. Li (2011), Real-time measurement and preliminary analysis of debris-flow impact force at Jiangjia ravine, China, *Earth Surf. Process. Landf., 36,* 1268–1278.

Huang, N. E., Z. Shen, S. R. Long, et al. (1998), The empirical mode decomposition and the Hilbert spectrum for nonlinear and non-stationary time series analysis, *Proc. R. Soc. A, 454*(1971), 903–995.

Hubl, J., J. Suda, D. Proske, R. Kaitna, and C. Scheidl (2009), Debris flow impact estimation, In *Eleventh international symposium on water management and hydraulic Engineering,* vol. 1, pp. 137–148, Ohrid, Mazedonien.

Hungr, O., G. C. Morgan, and R. Kellerhals (1984), Quantitative analysis of debris torrent hazard for design of remedial measures, *Can. Geotech. J., 21,* 663–677.

Itoh, R., and T. Hatano (2019), Geological implication of grain-size segregation in dense granular matter, *Philos, Trans. R. Soc. A-Math. Phys. Eng. Sci., 377* (2136).

Iverson, R. M. (1997), The physics of debris flows, *Rev. Geophys., 35(3),* 245–296.

Iverson, R. M. (2003), *Debris Flow Mechanics and Mitigation Conference,* chap. The debris–flow rheology myth, pp. 303–314, Mills Press, Davos.

Iverson, R. M., M. E. Reid, M. Logan, R. G. LaHusen, J. W. Godt, and J. P. Griswold (2011), Positive feedback and momentum growth during debris-flow entrainment of wet bed sediment, *Nature Geosci., 4,* 116–121.

Iverson, R. M., D. L. George, and M. Logan (2016), Debris flow runup on vertical barriers and adverse slopes, *J. Geophys. Res. Earth Surf., 121,* 2333–2357.

Johnson, C. G., B. P. Kokelaar, R. M. Iverson, M. Logan, R. G. Lahusen, and J. M. N. T. Gray (2012), Grain-size segregation and levee formation in geophysical mass flows, *J. Geophys. Res.-Earth Surf., 117,* F01032.

Kaitna, R., M. C. Palucis, B. Yohannes, K. M. Hill, and W. E. Dietrich (2016), Effects of coarse grain size distribution and fine particle content on pore fluid pressure and shear behavior in experimental debris flows, *J. Geophys. Res.-Earth Surf., 121,* 415–441.

Levy, A., and M. Sayed (2008), Numerical simulations of the flow of dilute granular materials around obstacles, *Powder Technol., 181(2),* 137–148.

Maheshwari, S., and A. Kumar (2014), Empirical Mode Decomposition: Theory & Applications, International Journal of Electronic and Electrical Engineering, 7(8), 873–878.

May, L. B. H., L. A. Golick, K. C. Phillips, M. Shearer, and K. E. Daniels (2010), Shear-driven size segregation of granular materials: Modeling and experiment, *Phys. Rev. E, 81* (5), 051301.

McCoy, S. W., J. W. Kean, J. A. Coe, D. M. Staley, T. A. Wasklewicz, and G. E. Tucker (2010), Evolution of a natural debris flow: In situ measurements of flow dynamics, video imagery, and terrestrial laser scanning, *Geology, 38,* 735–738.

Parsons, J. D., K. X. Whipple, and A. Simoni (2001), Experimental study of the grain-flow, fluid-mud transition in debris flows, *Geology 109 (4),* 427–447.

Pierson, T. C. (2005), *Distinguishing Between Debris Flows and Floods From Field Evidence in Small Watersheds,* US Dep. of the Int., U.S. Geol. Survey, Reston, Va.

Pudasaini, S. P. (2012), A general two-phase debris flow model, *J. Geophys. Res.-Earth Surf., 117,* F03010.

Pudasaini, S. P., and J. T. Fischer (2020), A mechanical model for phase separation in debris flow, *Int. J. Multiph. Flow, 129,* 103292.

Roche, O., Y. Nino, A. Mangeney, B. Brand, N. Pollock, and G. A. Valentine (2013), Dynamic pore-pressure variations induce substrate erosion by pyroclastic flows, *Geology, 41,* 1107–1110.

Savage, S. B., and K. Hutter (1989), The motion of a finite mass of granular material down a rough incline, *J. Fluid Mech., 199,* 177–215.

Scheidl, C., M. Chiari, R. Kaitna, M. Mullegger, A. Krawtschuk, T. Zimmermann, and D. Proske (2013), Analysing debris-flow impact models, based on a small scale modelling approach, *Surv. Geophys., 34,* 121–140.

Song, D., G. Zhou, X. Chen, J. Li, A. Wang, P. Peng, and K. Xue (2021), General equations for landslide-debris impact and their application to debris-flow flexible barrier, *Eng. Geol., 288,* 106154.

Sovilla, B., M. Schaer, M. Kern, and P. Bartelt (2008), Impact pressures and flow regimes in dense snow avalanches observed at the Vallée de la Sionne test site, *J. Geophys. Res.-Earth Surf., 113,* F01010.

Staron, L., and J. C. Phillips (2015), Stress partition and microstructure in size-segregating granular flows, *Phys. Rev. E, 92(2),* 022210.

Takahashi, T. (2007), *Debris Flows: Mechanics, Prediction and Countermeasures, Proc. Monogr. Eng. Water Earth Sci.,* Taylor and Francis, Leiden.

Tiranti, D., S. Bonetto, and G. Mandrone (2008), Quantitative basin characterisation to refine debris-flow triggering criteria and processes: an example from the Italian Western Alps, *Landslides, 5(1),* 45–57.

Vallance, J. W., and S. B. Savage (2000), *Particle size segregation in granular flows down chutes*, In IUTAM symposium segregation in granular materials, vol. 81, pp. 31–51, Springer, Dordrecht, Netherlands.

Vanoni, V. A. (1975), *Sedimentation Engineering,* Am. Soc. of Civil Eng., New York.

Watanabe, M., and H. Ikeya (1981), *Investigation and analysis of volcanic mudflows on Mt. Sakurajima, Japan,* In Proc. Symp. on erosion and sediment transport measurements, vol. 133, pp. 245–256, IAHS Publ, Florence.

Weinhart, T., S. Luding, and A. R. Thornton (2013), *From discrete particles to continuum fields in mixtures,* In Proceedings of the 7th international conference on micromechanics of granular media, vol. 1542, pp. 1202–1205, AIP Publishing LLC, Sydney.

Zanuttigh, B., and P. Ghilardi (2010), Segregation process of water-granular mixtures released down a steep chute, *J. Hydrol. 391(1–2),* 175–187.

Zheng, H., Z. Shi, M. Peng, and S. Yu (2018), Coupled CFD-DEM model for the direct numerical simulation of sediment bed erosion by viscous shear flow, *Eng. Geol., 245,* 309–321.

Zheng, H., Z. Shi, D. Shen, M. Peng, K. J. Hanley, C. Ma, and L. Zhang (2021a), Recent advances in stability and failure mechanisms of landslide dams, *Front. Earth Sci., 9,* 659935.

Zheng, H., Z. Shi, K. J. Hanley, M. Peng, S. Guan, S. Feng, and K. Chen (2021b), Deposition characteristics of debris flows in a lateral flume considering upstream entrainment, *Geomorphology, 394*: 107960.

Zheng, H., Z. Shi, S. Yu, X. Fan, K. J. Hanley, and S. Feng (2021c), Erosion mechanisms of debris flow on the sediment bed, *Water Resour. Res., 57(12)*: WR030707.

Zhou, G. G. D., K. F. E. Cui, L. Jing, T. Zhao, D. Song, and Y. Huang (2020), Particle size segregation in granular mass flows with different ambient fluids, *J. Geophys. Res.-Solid Earth, 125* (10)*,* e2020JB019536.

Supplementary Information for "Characteristics of the impact pressure of debris flows"

Hongchao Zheng[1], Zhenming Shi[1], Tjalling de Haas[2], Danyi Shen[1*], Kevin J Hanley[3], Bo Li[1]

[1]Department of Geotechnical Engineering, College of Civil Engineering, Tongji University, China

[2] Department of Physical Geography, Utrecht University, The Netherlands

[3]School of Engineering, Institute for Infrastructure and Environment, The University of Edinburgh, United Kingdom
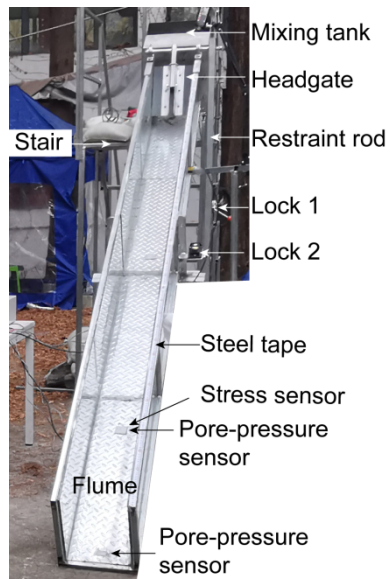
Contents:

Figure S1. Experimental apparatus consisting of a mixing tank, lever system and straight-slope flume. After lock 1 was opened, the headgate swung open horizontally within ~0.5 seconds and was held automatically by lock 2 mounted on the flume sidewall. This initiation process was similar to simple pendulum motion.
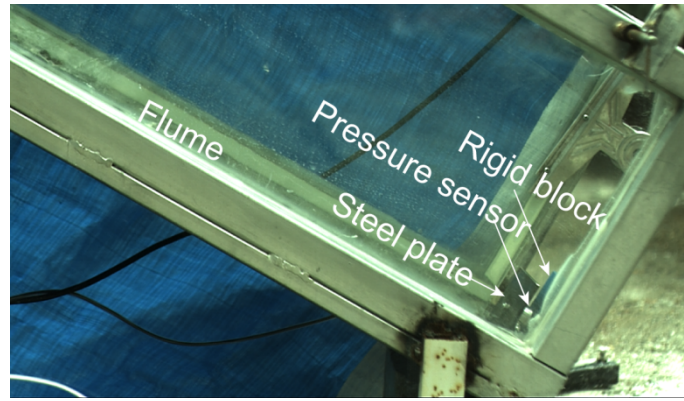
Figure S2. Pressure sensor to measure the impact pressure of a debris flow. The pressure sensor was located between the steel plate and the rigid block. A cylindrical strain-gauge sensor was used to measure the impact pressure at the flume exit. A square steel plate (80 mm × 80 mm) was mounted to the strain-gauge sensor to bear the impact pressure. The size of this plate was ten times larger than the maximum debris grain size (8 mm) in order to eliminate the stress concentration of coarse grains.
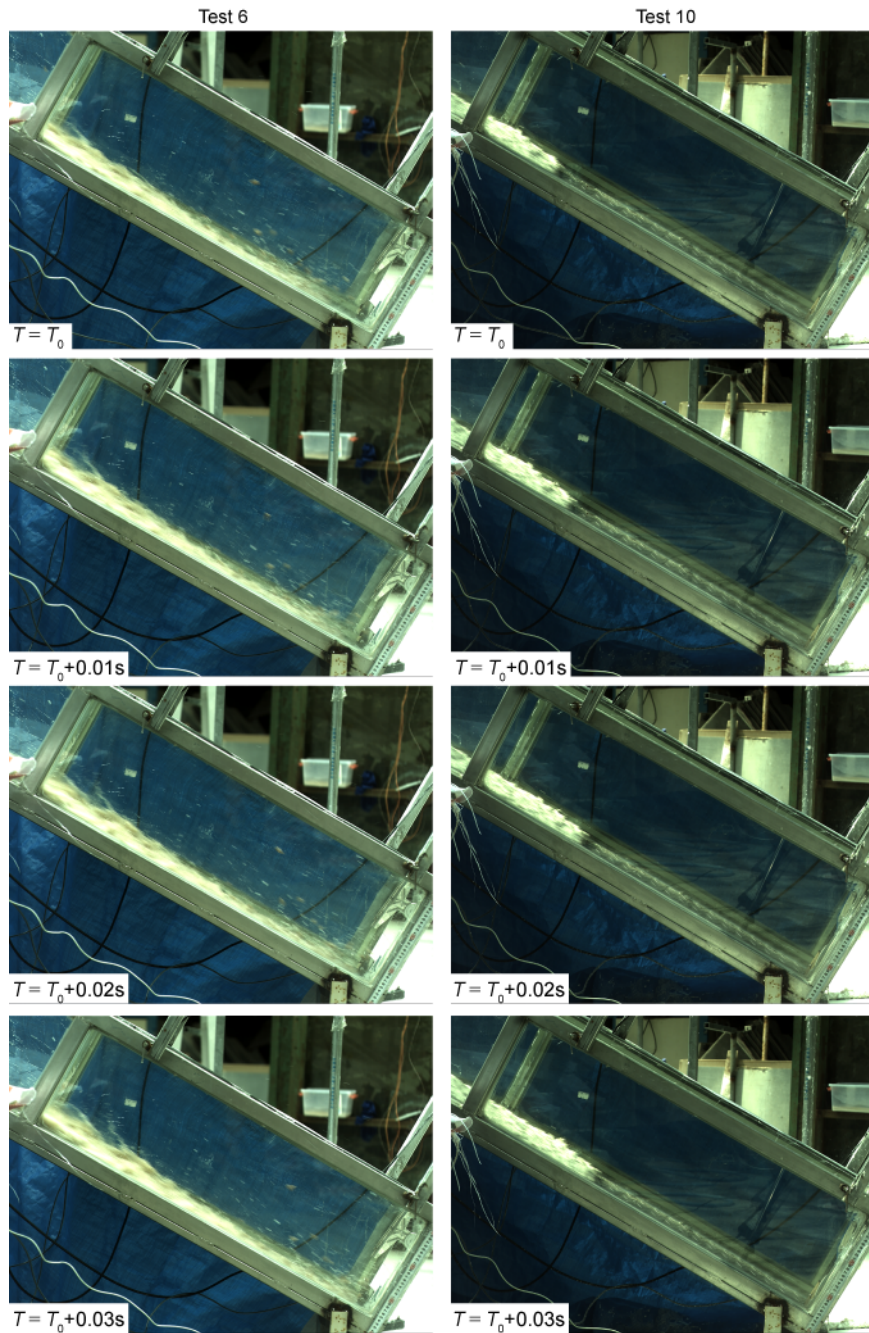
Figure S3. Flow characteristics in tests 6 and 10 from side view. The released flow in test 6 tumbled downwards. By contrast, the released flow in test 10 behaved similarly to a plug flow in the depth direction. T_0 is the time corresponding to the first frame.
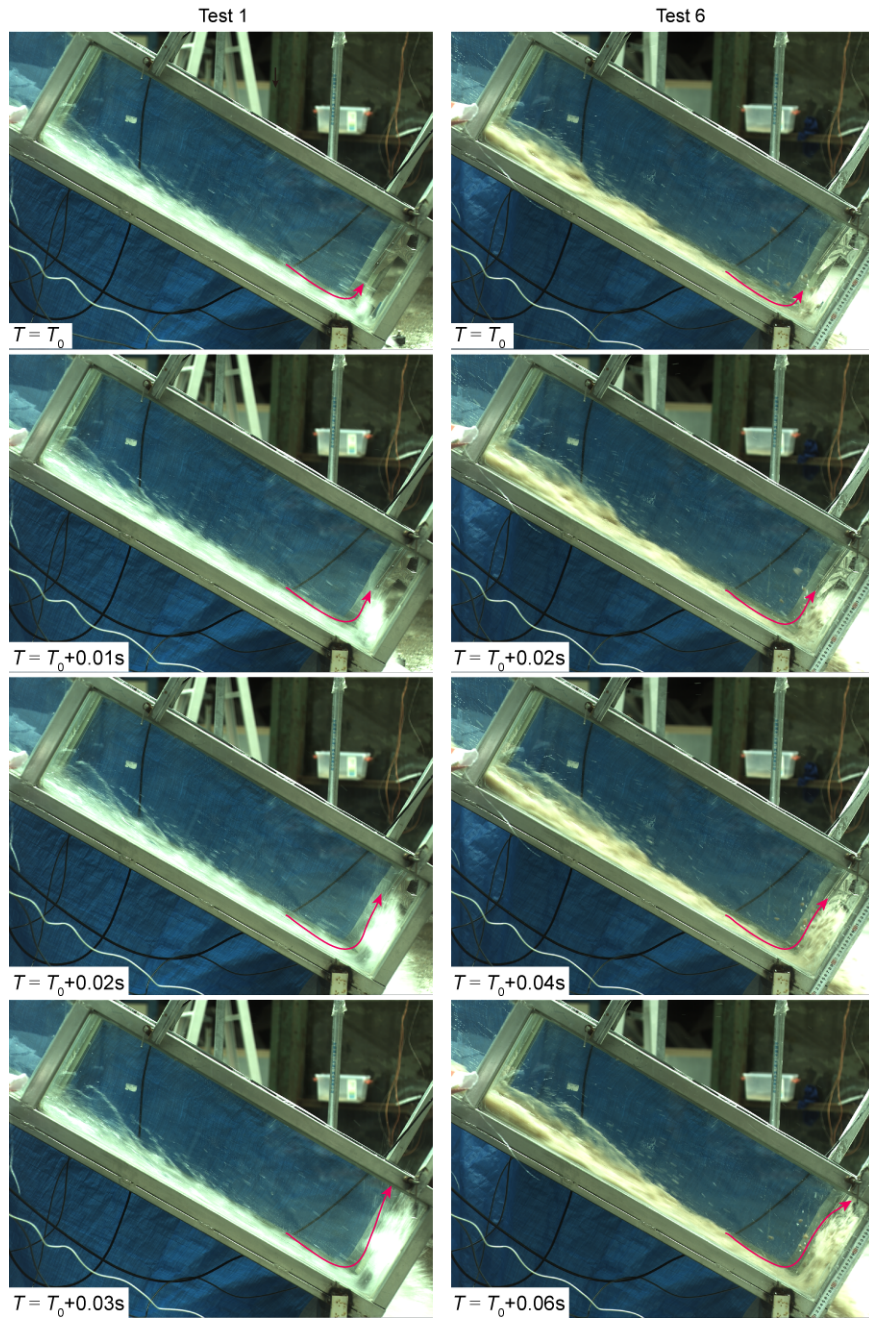
Figure S4. Impact process of released flows in tests 1 and 6 from side view. The released flows impacted the steel plate mounted to the pressure sensor and were diverted upwards parallel to the plate, producing a jet-like flow at the flume exit.
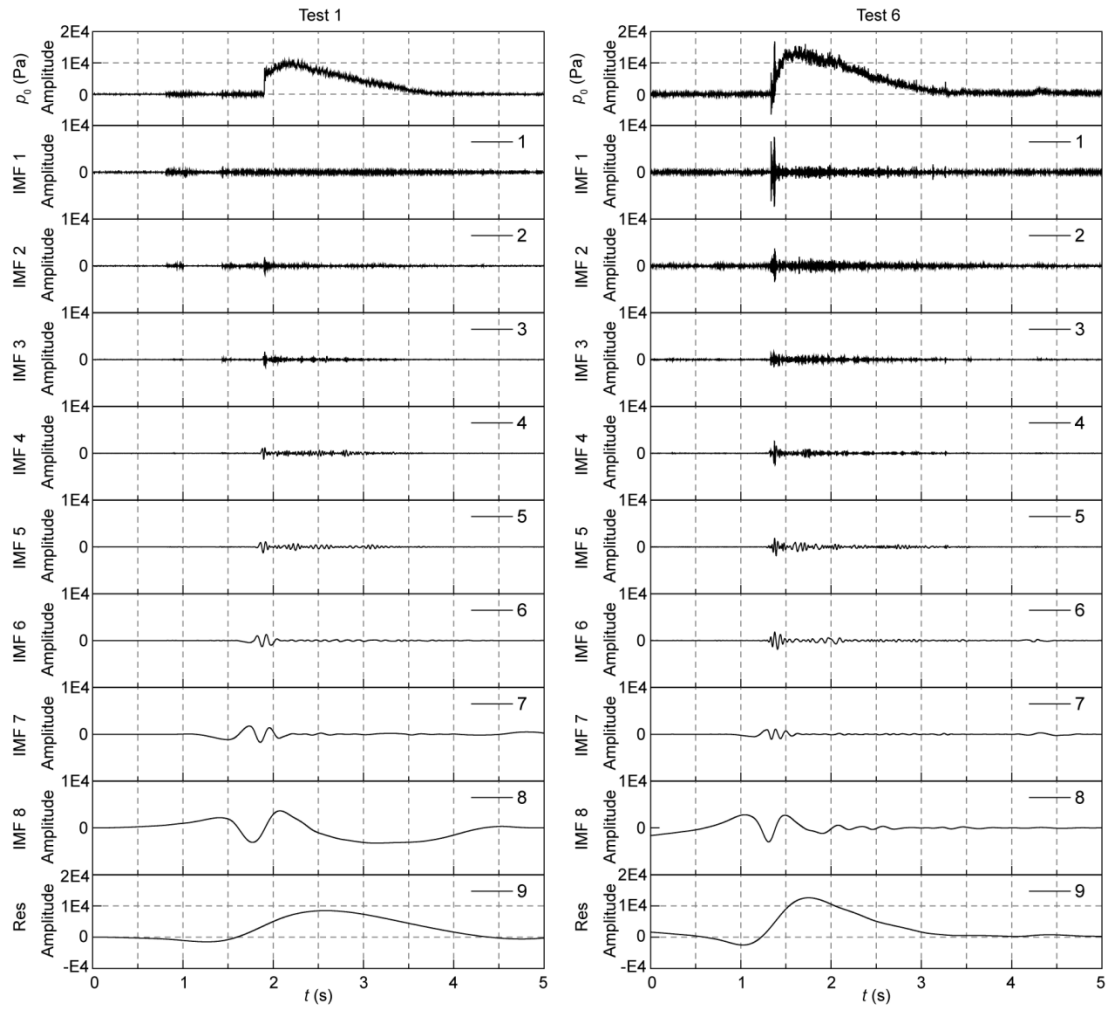
Figure S5. Decomposition of impact pressure signals by means of EMD during tests 1 and 6.
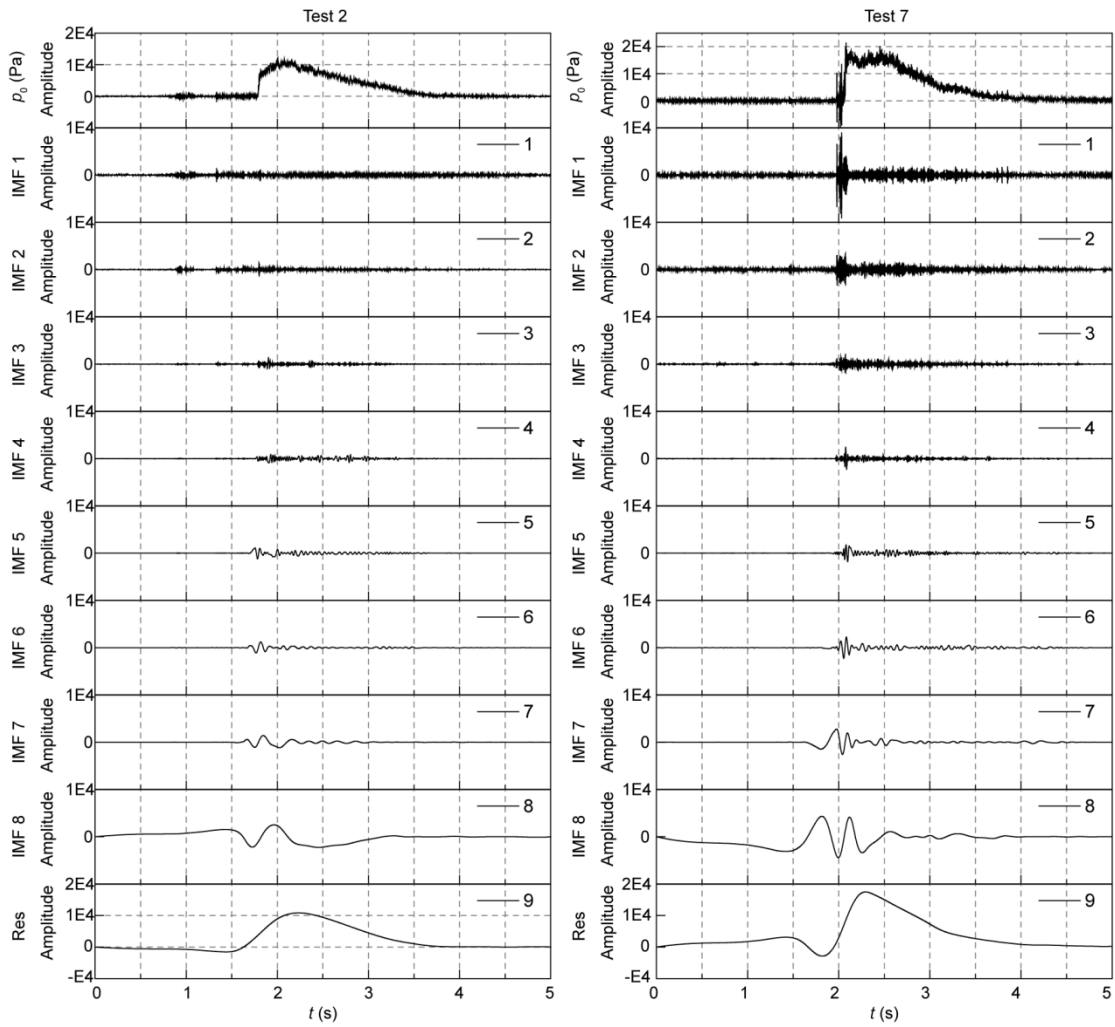
Figure S6. Decomposition of impact pressure signals by means of EMD during tests 2 and 7.
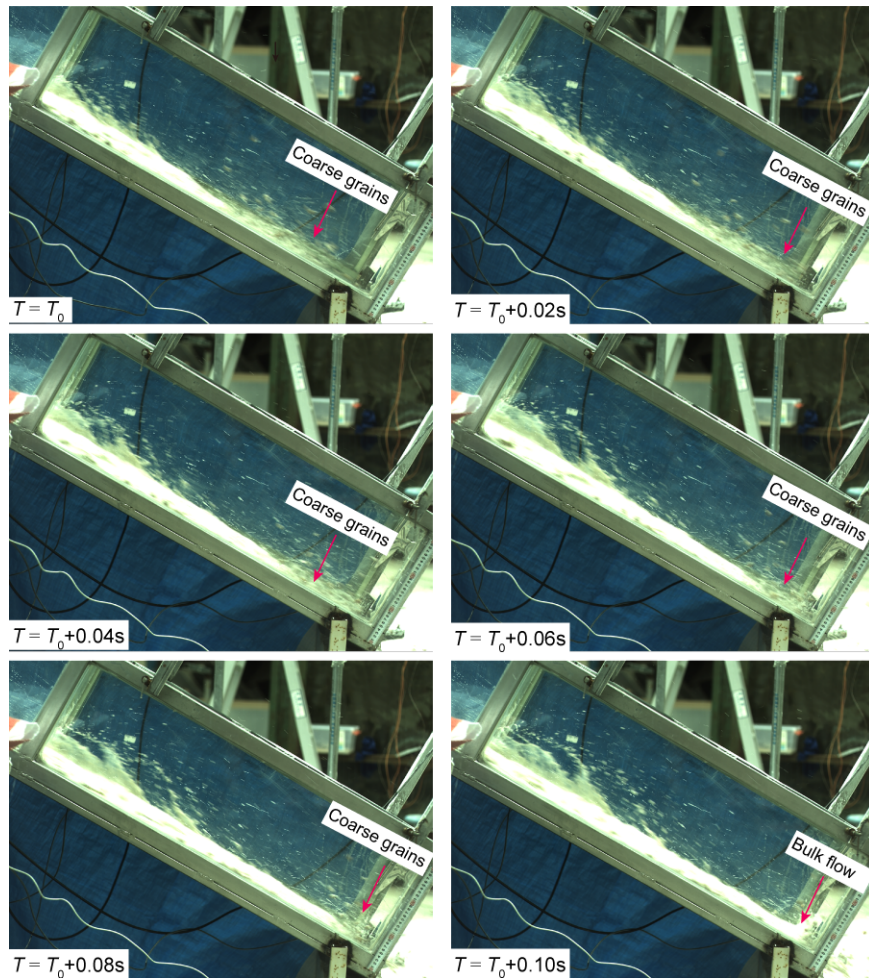
Figure S7. Impact process of debris flows in test 7. The coarse grains ahead of the bulk flow impacted the sensor, generating a local fluctuation of high frequency (Figure S6). 0.08 seconds later, the bulk flow reached the sensor, generating an impact pressure consisting of stationary mean pressure and local fluctuation components. T_0 is the time corresponding to the first frame.

Figure S8. Recomposition of impact pressure p_b with stationary mean pressure p_m and local fluctuations p_c from the hard impact of coarse grains in tests 2 and 7.

Empirical mode decomposition

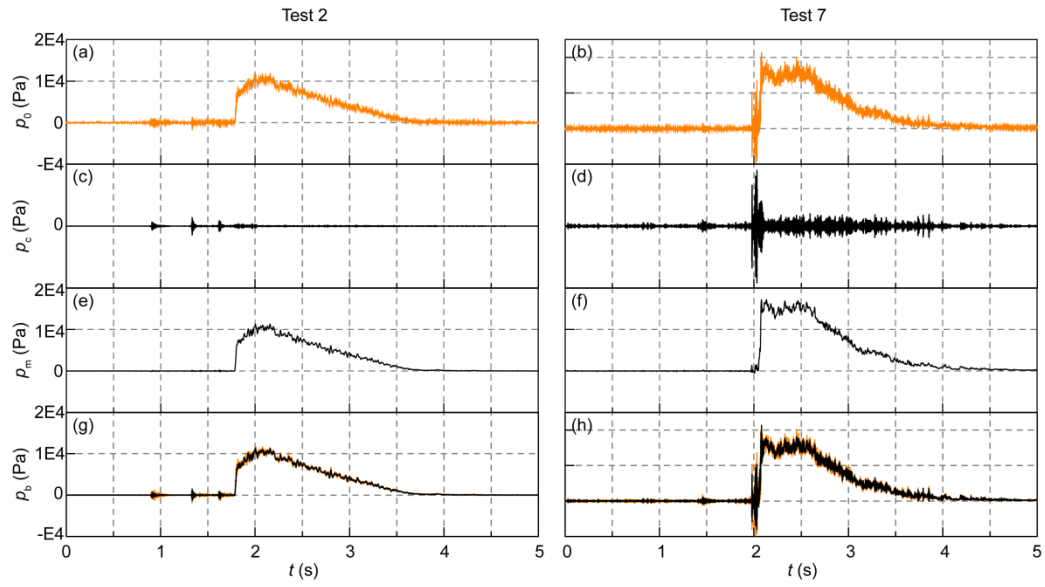Empirical mode decomposition (EMD) is a relatively new method proposed by Huang et al. [1998] for decomposing non-linear and non-stationary signals into a series of intrinsic mode functions (IMFs). An IMF represents the repeating behavior of the signal at some particular time scale. A time signal can be reduced to a set of basis signals with EMD.

Fourier transforms and wavelet transforms decompose the signal into a weighted sum of sinusoids for efficient extraction of information [*Maheshwari and Kumar,* 2014]. By contrast, the basis functions are derived from the data itself for EMD. Consequently the results preserve the full non-stationarity of the signal under consideration. The instantaneous frequency and amplitude of the signal can be obtained when a Hilbert transform is applied to the IMFs. The advantage of the method is that it is totally adaptive and data driven, without a priori basis function selection for signal decomposition.

Signal decomposition is conducted with MATLAB (The MathWorks, version R2018a). The steps are as follows:

(1) Extract all the local maxima and minima of $p_0(t)$.

(2) Form the upper and lower envelopes $e_u(t)$ and $e_l(t)$ by cubic spline interpolation of the extrema points extracted in step (1).

(3) Calculate the mean function of the upper and lower envelopes, $m_1(t)$ as $m_1(t) = 0.5(e_l(t) + e_u(t)$.

(4) Let $d_1(t) = p_0(t) - m_1(t)$. The iterations stop when $d_1(t)$ is a zero-mean function and $d_1(t)$ is accepted as first IMF, i.e., $IMF_1(t) = d_1(t)$.

(5) If not, use $d_1(t)$ as the new data and repeat steps 1–4 until ending up with an IMF.

Maximum Stationary Mean Pressures

The head form of the Bernoulli equation applied to a streamline is

$$z_1 + \frac{p_1}{\rho_b g} + \frac{u_1^2}{2g} = z_2 + \frac{p_2}{\rho_b g} + \frac{u_2^2}{2g} + h_f \tag{S1}$$

where h_f is the head loss between section 1 and section 2. The bulk density, ρ_b, is assumed to be equal at the two sections. u_1 and u_2 are the flow velocities in the depth direction at sections 1 and 2, respectively. According to the continuity equation,

$$dQ = u_1 dA_1 = u_2 dA_2 \tag{S2}$$

where Q is the flow rate, and A_1 and A_2 are the cross-sectional areas at sections 1 and 2, respectively.

The energy equation of a section per unit time is

$$\left(z_1 + \frac{p_1}{\rho_b g} + \frac{u_1^2}{2g} \right) \rho_b g \, dQ = \left(z_2 + \frac{p_2}{\rho_b g} + \frac{u_2^2}{2g} \right) \rho_b g \, dQ + h_f \rho_b g \, dQ \tag{S3}$$

By integration on the section,

$$\int_{A_1} \left(z_1 + \frac{p_1}{\rho_b g} \right) \rho_b g u_1 \, dA_1 + \int_{A_1} \frac{u_1^3}{2g} \rho_b g \, dA_1$$
$$= \int_{A_2} \left(z_2 + \frac{p_2}{\rho_b g} \right) \rho_b g u_2 \, dA_2 + \int_{A_2} \frac{u_2^3}{2g} \rho_b g \, dA_2 + \int_Q \rho_b g h_f \, dQ \tag{S4}$$

Assuming a hydrostatic pressure distribution in the depth direction, the piezometric head $\left(z + \dfrac{p}{\rho_b g} \right)$ at a cross section in the z direction, with reference to Figure S9, is constant. Thus, Equation (S4) can be expressed as

$$\left(z_1 + \frac{p_1}{\rho_b g} \right) \int_{A_1} u_1 dA_1 + \int_{A_1} \frac{u_1^3}{2g} dA_1$$
$$= \left(z_2 + \frac{p_2}{\rho_b g} \right) \int_{A_2} u_2 dA_2 + \int_{A_2} \frac{u_2^3}{2g} dA_2 + \int_Q h_f dQ \tag{S5}$$

The correction coefficient of flow kinetic energy α is defined as

$$\alpha \frac{v^2}{2g} = \frac{1}{Q} \int_A \frac{u^3}{2g} dA \tag{S6}$$

where v is the mean flow velocity in the depth direction. Equations (S5) and (S6)

lead to

$$z_1 + \frac{p_1}{\rho_b g} + \frac{\alpha_1 v_1^2}{2g} = z_2 + \frac{p_2}{\rho_b g} + \frac{\alpha_2 v_2^2}{2g} + h_f \tag{S7}$$

The incident flow front close to the obstacle is taken as section 1 and the top of the jet

flow is taken as section 2. h_f is ignored, considering an instantaneous impact process,

and Equation (S7) is reduced to Equation (6). The piezometric head is constant at all

points across section 1 and is equal to $h_1 \cos\theta$ where h_1 is the flow depth of the

incident flow at the front. On the reference plane where $z_1 = 0$, the hydrostatic

pressure $p_1 = \rho_b g h_1 \cos\theta$. Section 2 is located at the top of the flow where the flow

depth in the z direction (Figure S9) is h_2. The piezometric head for section 2 is

$h_2 \cos\theta$. On the reference plane, $z_2 = 0$ and the hydrostatic pressure $p_2 = \rho_b g h_2 \cos\theta$.

$v_2 = 0$ at the top of the flow.

By substitution into Equation (6),

$$\frac{h_2}{h_1} = 1 + 0.5\alpha_1 \left(\frac{v_1}{\sqrt{gh_1 \cos\theta}} \right)^2 = 1 + 0.5\alpha_1 F_r^2 \tag{S8}$$

Since the hydrostatic pressures along the reference plane are known, the impact

pressure p_2 can be expressed as

$$p_2 = p_1\left(1+0.5\alpha_1 F_r^2\right) \qquad\qquad \text{(S9)}$$

The mean impact pressure exerted on the steel plate

$$p_w = p_2 - \rho_b g h_o \qquad\qquad \text{(S10)}$$

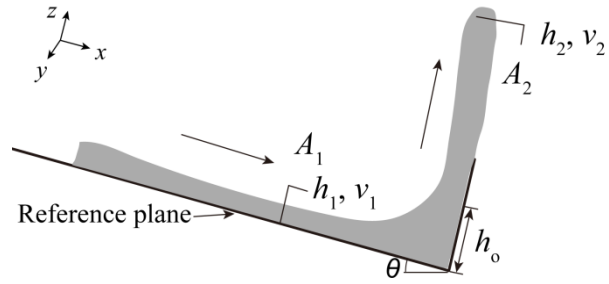where h_o is the vertical distance from the panel center to the flume bottom.

Figure S9. Illustration of analytical model for flow impact against a steel plate.

Table S1 Measured values for flows in each test

Test	v (m/s)	h (cm)	F_r	γ (/s)	p_{mm} (Pa)	p_w (Pa)	LR	p_{cm} (Pa)
1	4.75	0.055	6.85	86.4	10594	11173	–	–
2	4.70	0.055	6.78	85.5	11243	12031	–	–
3	4.75	0.055	6.85	86.4	12087	13408	–	–
4	4.60	0.050	6.96	92.0	12198	13557	–	–
5	4.20	0.045	6.70	93.3	10809	11643	–	–
6	4.10	0.060	5.66	68.3	14053	14098	0.59	7561
7	4.50	0.060	6.21	75.0	17149	17586	0.67	8970
8	4.90	0.060	6.77	81.7	22450	21569	0.68	12334
9	4.35	0.055	6.27	79.1	16672	17468	0.73	8279
10	3.80	0.050	5.75	76.0	11839	13427	0.83	2733
11	3.70	0.070	4.73	52.9	12209	12100	0.40	3905
12	4.45	0.065	5.90	68.5	20460	17913	0.51	6687
13	4.70	0.060	6.49	78.3	22241	20507	0.74	7784
14	4.30	0.060	5.94	71.7	16686	17668	0.96	4053
15	3.50	0.055	5.05	63.6	9438	11772	0.72	2717
16	3.30	0.070	4.22	47.1	11248	10033	0.29	4430
17	4.00	0.065	5.31	61.5	16107	15002	0.69	6250
18	4.50	0.055	6.49	81.8	20807	19323	0.60	8341
19	4.30	0.060	5.94	71.7	18070	18189	0.87	4790
20	2.85	0.050	4.31	57.0	5693	7893	0.76	2111

Note: v and h are the mean flow velocity and depth at the flow front, respectively. p_{mm} is the maximum stationary mean pressure, and p_{cm} is the maximum fluctuating pressure from the collision of coarse grains. The liquefaction ratio (LR) of a debris flow is defined as the basal pore pressure, p (t), divided by the total normal stress, σ_t (t). Considering the unsteady flow behavior during motion, LR in Table S1 is obtained when the maximum σ_t (t) is reached. LR generally increases with slurry density. The LR of debris flow with ρ_s = 1300 kg/m^3 and 1350 kg/m^3 is approximately 0.8, indicating that the debris grains have been significantly liquefied. The presence of coarse grains (5–8 mm) can increase local normal stress due to point-wise loading [*Scheidl et al.,* 2013]. This phenomenon cannot be completely eliminated by filtering. The measured peak basal normal stresses in tests 15 and 20 are higher than the actual values because point-wise loading occurs at maximum σ_t (t), resulting in a lower LR.

References

Huang, N. E., Z. Shen, S. R. Long, et al. (1998), The empirical mode decomposition and the Hilbert spectrum for nonlinear and non-stationary time series analysis, *Proceedings of the Royal Society A, Mathematical, Physical and Engineering Sciences, 454(1971)*, 903–995.

Maheshwari, S., and A. Kumar (2014), Empirical Mode Decomposition: Theory & Applications, *International Journal of Electronic and Electrical Engineering, 7(8),* 873–878.

Scheidl, C., Chiari, M., Kaitna, R., Mullegger, M., Krawtschuk, A., Zimmermann, T., and Proske, D. (2013), Analysing debris-flow impact models, based on a small scale modelling approach. *Surveys in Geophysics, 34,* 121–140.